

The use of satellite-measured aerosol optical depth to constrain biomass burning emissions source strength in a global model GOCART

Mariya Petrenko¹, Ralph Kahn², Mian Chin², Amber Soja^{3,4}, Tom Kucsera^{5,2}, Harshvardhan¹

- 1 Department of Earth and Atmospheric Sciences, Purdue University, West Lafayette, IN 47907, USA
- 2 Earth Science Directorate, NASA Goddard Space Flight Center, Greenbelt, Maryland, 20771, USA
- 3 National Institute of Aerospace, Hampton, Virginia, 23666, USA
- 4 NASA Langley Research Center, Hampton, Virginia, 23681, USA
- 5 Science Systems and Applications, Inc., Lanham, Maryland 20706

Correspondence:

Mariya Petrenko
NASA GSFC Code 613
Greenbelt, MD, 20771, USA
mshcherb@purdue.edu
301-614-6130

Abstract

Simulations of biomass burning (BB) emissions in chemistry transport models strongly depend on the inventories that define emission source locations and strength. In this work, we use 13 global biomass burning emission estimates, including the widely used Global Fire Emission Database (GFED) monthly and daily versions, Fire Radiative Power (FRP)-based Quick Fire Emission Dataset QFED, and 11 calculated emissions from different combinations of burned area based on the Moderate Resolution Imaging Spectroradiometer (MODIS) products, fuel consumption, and species emission factors as alternative inputs to the global Goddard Chemistry Aerosol Radiation and Transport (GOCART) model. The resultant simulated aerosol optical depth (AOD) and its spatial distribution are compared to AOD snapshots measured by the MODIS instrument for 124 fire events occurring between 2006 and 2007. It is shown that the quantitative relationship between BB emissions and model-simulated AOD is related to the horizontal plume dispersion, which can be approximated by the wind speed in the planetary boundary layer in most cases. Thus, given average wind speed of the smoke plume environment, MODIS-measured AOD can provide a constraint to the strength of BB sources. In addition, we compare selected global BB emission estimates and review their regional performance when used in the GOCART model. The limitations of using MODIS AOD snapshots to constrain biomass burning source strength in the global aerosol models are also discussed.

1 Introduction

Biomass burning (BB) has been recognized as one of the major contributors to carbonaceous aerosol emissions of black carbon (BC) and organic carbon (OC), as well as a source of aerosol precursor gases such as SO₂, NO_x, and a suite of volatile organic compounds [Akagi *et al.*, 2011; Andreae and Merlet, 2001]. Optically and chemically potent biomass burning particles play important roles in atmospheric processes through their impact on air quality [NARSTO, 2003; Sapkota *et al.*, 2005; Wiedinmyer *et al.*, 2006], visibility [Bäumer *et al.*, 2008; Mazurek *et al.*, 1997] and human health [Seaton *et al.*, 1995], and as one of the factors affecting global climate through direct and indirect radiative effects [IPCC, 2007; Lohmann and Feichter, 2005; Yu *et al.*, 2006]. Therefore, it is important to represent biomass burning emissions as accurately as possible in global and regional models, which are among the main tools for studying earth and atmospheric processes [CCSP, 2009], estimating climate forcings [Boucher and Anderson, 1995; Dentener *et al.*, 2005; IPCC, 2007], and assessing both regional pollution loads [Quinn *et al.*, 2008; Shindell *et al.*, 2008] and long-range transport of pollutants [Chin *et al.*, 2007; Colarco *et al.*, 2004; Damoah *et al.*, 2004; Jaffe *et al.*, 2004; Warneke *et al.*, 2009].

To simulate the emission and subsequent evolution and transport of aerosol particles from fires, models need two essential pieces of information - strength of the biomass burning sources and height of injection. Location and strength of BB sources are usually input into the model from an external emission inventory. A number of global and regional BB emission inventories exist, and are usually constructed bottom-up, considering the properties of the burning ecosystem and the extent and properties of the fires [Giglio *et al.*, 2006b; Ito and Penner, 2004; Lioussé *et al.*, 2010; Michel *et al.*, 2005; Turquety *et al.*, 2007; Van der Werf *et al.*, 2010; Vermote *et al.*,

2009; *Wiedinmyer et al.*, 2011]. Alternatively, a top-down approach, described, for example, by *Dubovik et al.* [2008], uses inverse modeling to estimate biomass burning source strength from the measured aerosol properties, such as aerosol optical depth (AOD). This latter approach is labor- and computation-intensive, and is not widely used by the aerosol modeling community.

Natural BB variability [*Schultz et al.*, 2007; *Van der Werf et al.*, 2006], errors and uncertainties associated with the estimates and measurements of emission-related parameters, such as (1) burned area [*Giglio et al.*, 2010], (2) biomass type and properties [*Fritz and See*, 2008], (3) aerosol and gas emission factors [*Akagi et al.*, 2011], (4) properties of the fire and environment in which burning happens [*Hyer and Reid*, 2009; *Soja et al.*, 2004; *Van der Werf et al.*, 2010], as well as (5) different approaches to calculating emissions [*Al-Saadi et al.*, 2008] - all lead to discrepancies between emission estimates provided by BB emission inventories. These discrepancies can be quite significant, and they propagate in aerosol models to impact simulated aerosol effects [*Chin et al.*, 2009; *Reid et al.*, 2009].

The amount of aerosol in the atmospheric column is directly proportional to AOD observed at the top of the atmosphere [*Levy et al.*, 2007, 2010]. AOD is routinely measured by spaceborne instruments. Each such measurement captures the aggregation of aerosol particles that have been emitted into the atmosphere by the fires, from the beginning of burning until the time of measurement, except those that were transported away from the field of view. It is, therefore, possible to use satellite-measured AOD as an instantaneous observational constraint to the strength of biomass burning sources in an aerosol model.

In this work, we use 13 global biomass burning emission estimates, including the widely used Global Fire Emission Database (GFED) monthly and daily versions, Fire Radiative Energy (FRE)-based Quick Fire Emission Dataset QFED, and 11 calculated emissions from different

combinations of burned area based on the Moderate Resolution Imaging Spectroradiometer (MODIS) products, fuel consumption, and species emission factors as alternative inputs to the global Goddard Chemistry Aerosol Radiation and Transport (GOCART) model. The resultant simulated AOD and its spatial distribution are compared to AOD snapshots measured by the MODIS instrument for 124 fire events occurring between 2006 and 2007, providing information on how satellite AOD data can be used to constrain the BB emission. We describe the approach, emission datasets, GOCART model, and satellite observations in sections 2 and 3, and show the model results of AOD from different emission estimates and discuss the outcome in section 4. Conclusions from this study are given in section 5.

2 Estimation of biomass burning source strength

2.1 Estimating BB emissions based on burned area

The most common way to estimate BB emissions is the following empirical relationship, which is based on the one originally introduced by Seiler & Crutzen [1980]:

$$M_j = A * B * \beta * F_j, \quad [1]$$

where M_j is the mass of emitted species j (here BC, OC, and SO_2); A is the burned area; B is the average amount of biomass or organic matter an ecosystem contains per unit area; β is the combustion completeness or burning efficiency, which is the fraction of fuel actually consumed in a fire [Soja *et al.*, 2004; Van der Werf *et al.*, 2006]. β is dependent on the fire severity and fuel type, and can range from 98% for standing dry grass to less than 10% for dead logs [Lioussé *et al.*, 2003]; and F_j is the emission factor of species j , defined as the amount of species j released per unit of fuel consumed [Andreae and Merlet, 2001], expressed in grams of tracer per kilogram of burned dry mass.

The product of A , B and β in Equation 1 represents the amount of fuel consumed within the burned area, or “dry mass burned (DM)”, and the product of fuel density B and combustion completeness β the “fuel consumption”. Listed below are several data products that provide estimates of each term in Equation 1 individually or as part of a combined quantity, e.g., fuel consumption or dry mass burned. These data products are later combined to provide BB emissions to the aerosol model.

2.1.1 Burned area (A)

a) *The MODIS collection 5 burned area product - MCD45A1* [Roy et al., 2008]: This product is developed based on the change of surface reflectance following a fire. The data are available from the Earth Observing System Clearing House [EOSDIS, 2009] in a set of monthly files, each containing one of the $\sim 10^\circ(\text{lat}) \times 10^\circ(\text{lon})$ granules defined on the MODIS sinusoidal grid [Giglio, 2010]. Each granule contains the locations of burned pixels for each day of the month, at 500 m spatial resolution, which were gridded to the $1^\circ(\text{lat}) \times 1.25^\circ(\text{lon})$ GOCART grid. Burned area estimates for the overlapping eight days before and after each month are ignored to avoid duplication. This product is referred to here as “MCD45.”

b) *Burned area estimated from MODIS active fire counts*: This product is based on the 1 km^2 size fire pixels from the combined MODIS-Terra (MOD14A1) and MODIS-Aqua (MYD14A1) thermal anomalies with multiple counting removed, i.e., pixels classified as fires more than once on the same day are counted only once. These data were also obtained from the EOS Clearing House [EOSDIS, 2009], and the fire counts were gridded to the $1^\circ(\text{lat}) \times 1.25^\circ(\text{lon})$ GOCART grid. This product is referred to here as “mod1”.

To estimate the area burned by the detected fires we assume that each pixel classified as burning corresponds to 1 km^2 of burned area. Here, we have to acknowledge the reported large

variations of effective burned area per detected fire, even in the same ecosystem [*Giglio et al.*, 2006b, 2009; *Roy et al.*, 2008; *Soja et al.*, 2004]. The conversion factors reported previously range from 0.3 km² to 6.6 km² effective burned area per fire detection, based solely on MODIS-Terra detection analyses in different locations globally [*Giglio et al.*, 2006b, 2010]. Other estimates include 0.79 km²/pixel [*Soja et al.*, 2009], and 0.625 km²/pixel [*Reid et al.*, 2009]. According to *Soja et al.* [2009], counting every pixel and assuming 1 km²/pixel for every fire detection leads to gross overestimation of burned area (by about a factor of 2 in the western US), highlighting the wide disparity in estimating burned area using fire detection data.

c) *Global Fire Emission Dataset version 3 (GFED3) burned area*: It is another MODIS-based product with 0.5°×0.5° spatial and daily temporal resolution [*Giglio et al.*, 2009]. The algorithm combines the detection of change in surface properties (vegetation index) with the use of the active fire product. Instructions on downloading GFED data and converting burned area from monthly to daily estimates are available from <http://globalfiredata.org/Data/index.html>.

2.1.2 Fuel density (B) and fuel consumption ($B \cdot \beta$)

a) *Global Land Cover dataset (GLC2000)*: Referred to here as "GLC", it provides a map of 22 land cover types globally, at the original 1-km and also a 0.5°×0.5° spatial resolution. GLC methodology and datasets are introduced by *Bartholome and Belward* [2005] and numerous subsequent publications [e.g., *Gonsamo and Chen*, 2011; *See and Fritz*, 2006; *Xiao-Peng et al.*, 2011], and available online at <http://bioval.jrc.ec.europa.eu/products/glc2000/glc2000.php>. Typical biomass density, combustion completeness, and emission factors are defined for 16 of the 18 vegetated land-cover types [*Lioussé et al.*, 2003, 2010; *Michel et al.*, 2005]. These properties are summarized in Table 1.

All emission calculations involving the GLC dataset were calculated with a spatial resolution of the original dataset ($0.5^{\circ} \times 0.5^{\circ}$) and then mapped onto the GOCART 1° (lat) x 1.25° (lon) grid. Figure 1 shows the spatial distribution of the vegetation types on the GOCART grid. The vegetation type occupying the largest areal fraction of each grid box is designated as dominant for that box and is the color shown on the map.

b) *The Weather- and Ecosystem-Based Fire Emissions* (WEB-FE): It is developed at the National Institute of Aerospace and NASA Langley Research Center, is available upon request from its developers (A. Soja). In this analysis, we use the Carbon Consumption (CC) database from WEB-FE, which is defined as the potential amount of available carbon consumed by fire.

Spatially-explicit fuel consumption estimates were first developed for Northern Eurasia based on the amount of fuel contained in ecosystems that could be available to burn [Soja *et al.*, 2004], which is ultimately dependent on the weather that precipitates fire events. Unique estimates for the potential amount of carbon (or fuel) consumed are calculated for 35 distinct ecoregions across Northern Eurasia, which includes 4 separate peatland estimates. Fuels data were taken from Alexeyev and Birdsey [1998] and include overstory, understory, litter, peat and soil organic matter; carbon is assumed to be 50% of the available fuel. Each ecoregion estimate consists of 3 potential severity classes, resulting in 105 discrete spatially-explicit estimates. For instance, a low-severity surface fire consumes 20% of the accessible understory and litter layer, and a high-severity crown fire consumes 20% of the accessible tree stand vegetation and 100% of the accessible understory and litter are consumed. Ecosystem-based estimates range from low-, medium- to high-severity carbon consumption and have been verified. Subsequently, the data were validated with ground-based fuel consumption data for a range of fire severities and ecosystems ($r^2=0.86$).

Global carbon consumption estimates were built from above-ground fuel provided by *Olson et al.* [1985] and soil carbon by *Zinke et al.* [1986], and these global estimates are overlaid with detailed data as they become available (currently for Northern Eurasia, Canada and Alaska). The global estimates were developed for near-real-time use and have proven themselves in numerous field campaigns [e.g., *Choi et al.*, 2008; *Pierce et al.*, 2007]. The information gleaned from this investigation will lead to improvements in this dataset.

The fuel consumption from biomass burning events is determined by the fire severity that is associated with the high, medium, and low CC data from WEB-FE. Here we use the Haines index (HI) to estimate the fire severity, which was developed to assess the potential for rapid fire growth [*Haines*, 1988] and is also known as the Lower Atmosphere Severity Index [*Winkler et al.*, 2007]. The Haines index is a number ranging from 2 to 6 that describes the stability and moisture content of the lower atmospheric layer (~1 km high) with topography taken into account. The index is a simple sum of two terms: the lapse rate term (temperature difference between layer bottom and top) describing the stability of the layer, and the Dewpoint depression term (difference between temperature and dew point temperature at the lower level). In other words, an unstable, dry atmosphere will have higher HI, indicating a likelihood of more severe fire. The HI was developed, and has been studied most extensively, for North America [*Werth and Ochoa*, 1993; *Winkler et al.*, 2007]; its application has not been evaluated for other parts of the world.

In this study HI was calculated for each GOCART grid box using 3-hourly reanalysis meteorological fields from the Goddard Earth Observing System version 4 Data Assimilation System (GEOS-4 DAS) [*Bloom et al.*, 2005], and the HI value determined the choice of the fuel consumption category from the CC datasets - HI of 2-4, 5, and 6 are associated with the low,

medium, and high CC, respectively. These 3-hourly CC values in each grid box were averaged over the course of 24 hours and then converted to fuel consumption (typically CC/0.5) for a particular day.

2.1.3 Emission factors (F_{ij})

In the standard GOCART configuration, emission factors of 1, 8, and 1.1 g per kg of burned dry mass are used globally for BC, OC and SO₂, respectively [Chin *et al.*, 2007]. Alternatively, for combinations that include GLC vegetation types, we use vegetation-type-dependent emission factors for BC, OC, and SO₂ provided in the GLC database (Table 1) [Lioussé *et al.*, 2003, 2010; Michel *et al.*, 2005].

The GFED emission inventory, introduced below, works with a set of vegetation type-dependent emission factors based on Andreae and Merlet [2001], which are used in some of the GOCART runs together with the GFED dry mass option. For comparison with other inventories, the GFED emission factors for the aerosol-related species of interest are given in Table 2, with the full set of species considered in GFED3, listed by Van der Werf *et al.* [2010]

2.2 Global Fire Emission Dataset (GFED) emission estimates

In addition to calculating the emissions from different components, as given in Equation 1, we also used emission estimates from GFED 3, which provides emission amounts ready to use in the models, or burned dry mass estimate ($DM=A*B*C$), which can be combined with different emission factor options. The GFED3 daily emission and burned dry mass at the original 0.5°×0.5° spatial resolution (<http://www.falw.vu/~gwerf/GFED/GFED3/emissions>) were re-gridded to the 1°(lat) × 1.25°(lon) GOCART grid. The GFED3 approach to estimating burned area combines deriving burned area from the change of surface properties with the use of fire detections in places where surface property information is unavailable [Giglio *et al.*, 2010]. The

Carnegie-Ames-Stanford-Approach (CASA) biogeochemical model used to estimate burned dry mass and emissions is described in detail by *Van der Werf et al.* [2010], and the method for scaling monthly GFED3 emissions to daily estimates using MODIS active fire counts is described by *Mu et al.* [2011].

GFED version 2 monthly emission estimates have been widely used in the aerosol modeling community [*Dentener et al.*, 2006], so this dataset is considered here to assess the potential changes with the switch to the newer version of GFED.

2.3 Estimating BB emission based on fire radiative energy (FRE)

The relationship between the energy released by the fire and emission of aerosols and gases was suggested by *Kaufman et al.* [1996], and has subsequently been studied and refined [*Ichoku and Kaufman*, 2005; *Schroeder et al.*, 2010; *Vermote et al.*, 2009; *Wooster et al.*, 2002, 2005]. The approach presented by *Wooster et al.* [2002, 2005] relates the amount of combusted biomass, which is equivalent to the term "dry mass burned (DM)" used in this study, and fire radiative energy (FRE) as follows:

$$DM \text{ (kg)} = a * FRE \text{ (MJ)}, \quad [2]$$

where a is an empirically derived factor. Fire radiative energy is the fire radiative power (FRP) obtained from the 3.9 μm wavelength radiative energy flux at the top-of-atmosphere measured by MODIS, and integrated over time for the estimated duration of burning. This relationship has been used by the developers of FRE-based emission inventories, such as Global Fire Assimilation System (GFAS, [*Kaiser et al.*, 2012]) and Quick Fire Emission Dataset (QFED, [*Darmenov and da Silva*, manuscript in preparation, 2012]) to estimate the amount of DM from the MODIS FRE. Species-specific emission factors are then applied to DM estimates to obtain

aerosol emissions. QFED developers omit the DM estimation step and work directly with emissions (using CO as a reference) to find coefficients that relate emission rates to FRP.

After the initial emissions have been estimated, these estimates are adjusted to improve the agreement between MODIS-measured AOD and model-simulated AOD by applying additional adjustments using MODIS AOD to specify region-specific emission strength [Darmenov and da Silva, manuscript in preparation, 2012]. QFED is the default BB emission inventory in the GEOS-5 modeling system [Rienecker *et al.*, 2008]. It provides daily estimates of BB emissions at $\sim 0.25^\circ(\text{lat}) \times 0.3125^\circ(\text{lon})$ horizontal resolution, and can be obtained from its developers at Global Modeling and Assimilations Office (GMAO, <http://gmao.gsfc.nasa.gov/>) at NASA Goddard Space Flight Center.

We use QFED version 2.2 in this study to compare its emission estimates with those by other inventories. Because QFED emissions are adjusted with the MODIS AOD, QFED-based GOCART runs are not used in model evaluations with MODIS AOD described in sections 4.2-4.4.

2.4 BB emission options

Ready-to-use emission inventories and the combinations of parameters, as described above, resulted in 13 datasets that define BB source location and strength. These products are referred to here as "emission options," and are summarized in Table 3. The name of the emission option is usually composed of three parts, where the first set of alphanumeric symbols stand for burned area product, next set of symbols signify the fuel consumption product, and the last symbols define the emission factor option. If the emissions came from a ready-to-use inventory (such as GFED3 or QFED), the name of the inventory is kept unchanged.

3 Aerosol from satellite observations and model simulations

3.1 GOCART model

GOCART is a global chemistry and transport model that simulates the major tropospheric aerosol types: sulfate and its precursors, OC, BC, dust, and sea salt. For this work, it uses assimilated meteorological fields from the GEOS-4 DAS [*Bloom et al.*, 2005] with a spatial resolution of 1.25° longitude by 1° latitude, and 30 vertical layers. The time step of model output is 3 hours.

The GOCART model is described in detail in several publications [e.g., *Chin et al.*, 2000, 2002, 2007, 2009; *Ginoux et al.*, 2001]. Briefly, chemical processes in the model include gas and liquid phase reactions that convert sulfate precursors (dimethylsulfide or DMS, and SO₂) to sulfate. Carbonaceous aerosol aging is represented by the conversion of hydrophobic aerosols (original 80% of BC and 50% of OC) to hydrophilic with an e-folding time of 2 days. Physical processes include aerosol emission, advection, convection, as well as wet and dry deposition. Biomass burning and anthropogenic emissions are input from available global inventories, and natural emissions are either from available estimates or calculated on-line as a function of meteorological conditions.

Biomass burning emissions of SO₂, BC, and OC are provided by external datasets summarized in section 2.4. The model was run once with each emission option, each time for the same 13 months (June 2006 - June 2007), preceded by a 3-month spin-up, with all other settings (e.g., anthropogenic and natural emissions) kept the same. Daily BB emissions were prepared off-line and then read into the model. All BB emissions were assumed to be injected within the planetary boundary layer.

Aerosol optical depth is determined from the dry mass concentrations and mass extinction coefficients for the major aerosol types, which are functions of aerosol size distributions, refractive indices, and humidity-dependent hygroscopic growth. Total AOD is the sum of optical depths of individual aerosol types: dust, black carbon, particulate organic matter, sulfate, and sea salt. The AOD calculation methods, as well as the sources and values of the relevant parameters, are described by *Chin et al.* [2002, 2009].

3.2 Satellite observations of aerosol

3.2.1 MODIS aerosol optical depth

MODerate resolution Imaging Spectroradiometer (MODIS) is a key instrument on board NASA's Terra and Aqua satellites. With a wide 2330 km swath, MODIS observes the whole globe in 1 to 2 days with a more frequent coverage of higher latitudes. Measurements made in 36 spectral bands between 0.405 and 14.385 μm are a source for a number of land, ocean and atmospheric products with band-dependent nominal spatial resolutions of 250 m, 500 m, or 1 km (<http://modis.gsfc.nasa.gov/about/>). We use here the 550 nm AOD from the MODIS Collection 5 level II aerosol product (MOD04 or MYD04 from the MODIS instruments on Terra and Aqua satellites, respectively) at 10 km resolution [*Levy et al.*, 2010; *Remer et al.*, 2006]. For each BB event, only one MODIS snapshot is used, from MOD04 or MYD04, as appropriate. All 10-km pixels where AOD retrievals are available are averaged to the $1^\circ\text{lat} \times 1.25^\circ\text{lon}$ GOCART grid for further comparison with the model AOD.

3.2.2 MISR stereo height and aerosol products

The Multiangle Imaging SpectroRadiometer (MISR) on board NASA's Terra satellite has a unique geometry, where it is looking down on Earth with nine cameras, precisely aligned to sequentially view a 380 km-wide swath at nine different angles in four spectral bands (blue,

green, red, and near-infrared), providing global coverage every 9 days [*Diner et al.*, 1998]. To evaluate the height of smoke layers we use the MISR operational level 2 stereo height product (from <http://eosweb.larc.nasa.gov>), which reports cloud and near-source aerosol plume heights globally, on a 1.1-km grid, and with vertical accuracy of about 0.5 km [*Moroney et al.*, 2002]. The MISR aerosol product includes AOD and aerosol type constraints globally [*Kahn et al.*, 2010], and is used here in some cases to confirm plume locations when assessing their height.

3.2.3 CALIPSO vertical feature mask

The CALIPSO satellite carrying the *CALIOP* (Cloud-Aerosol Lidar with Orthogonal Polarization) lidar system is a part of the ‘A-train’ constellation of sun-synchronous satellites, which cross the equator in the early afternoon around 1:30 P.M. local time in an ascending orbit. CALIPSO vertical feature mask provides vertical and horizontal distribution of cloud and aerosol layers with 5 km spatial resolution [*Vaughan et al.*, 2004; *Winker et al.*, 2009]. Aerosol and cloud layers are classified by associating measured optical or physical parameters (such as attenuated backscatter coefficient, or color ratio) with particular class of known atmospheric scatterer. Vertical Feature Mask is used here to evaluate smoke height in the studied cases, where CALIPSO observations are available. Daily CALIOP data are available at http://eosweb.larc.nasa.gov/PRODOCS/calipso/table_calipso.html.

3.3 Biomass burning events

One hundred and twenty four fire events, occurring between June 2006 and June 2007 in different regions of the world, were used to evaluate the emission options. These events include a range of fire sizes, seasons, types of vegetation, and burning conditions. Fire cases were selected to include smoke plumes, which are defined as smoke-like features appearing in MODIS visible images, supported by presence of fire pixels reported in MODIS thermal anomalies product

(MOD14/MYD14 for Terra and Aqua MODIS respectively), and at the same time showing elevated AOD in the MODIS AOD data. Thus, the sizes of study cases vary considerably, and can include single fires with associated smoke plumes, such as several events in the US, areas of generally hazy regions containing many fires with or without individual visible plumes, such as the agricultural burning in Africa, Eastern Europe or South America, or cases where large individual smoke plumes merge to produce thick smoke clouds, such as several cases in Russia, Canada, Indonesia, and South Australia. Table 4 provides a list of studied fire cases, which gives their unique identification numbers, specifies their geographic boundaries defined by latitude and longitude corners, reports the date of MODIS observation, and denotes the MODIS-carrying satellite used by letters "A" or "T", which stand for Aqua and Terra, respectively.

To locate the fire events, we used as a starting point events featured on the Earth Observatory web site, which provides a selection of fires in the Natural Hazards/Fires category (<http://earthobservatory.nasa.gov/NaturalHazards>). We also used a combination of MODIS visible browse images (<http://modis-atmos.gsfc.nasa.gov/IMAGES/>) and the locations of fire detections from the MOD14A1 and MYD14A1 thermal anomalies products to identify the locations and times of burning events. A subset of these events was chosen for analysis, based on whether smoke or general haziness, un-obscured by condensate cloud, appears in visible images of the region. Figure 1 displays a map showing the locations of the cases studied. They are grouped into geographic regions having roughly similar burning conditions.

In selecting the fire cases, we also considered biomass burning seasons in different regions. These seasons are described elsewhere [*Dey and Di Girolamo, 2010; Duncan et al., 2003; Giglio, 2010; Giglio et al., 2006a*] and are mentioned in Table 4. Table 4 also provides a description of prevailing vegetation and characteristics of burning in each world region.

In regions with strong dust sources, such as northern India and North Africa, we consider the seasonality of dust emissions as those times when dust significantly contributes to the total AOD. Much of the spring peak of forest and harvest burning in India coincides with the pre-monsoon dust season [*Dey and Di Girolamo, 2010*], so most burning cases are selected during early spring or during the smaller burning season in November. Similarly, major biomass burning in sub-equatorial Africa during boreal winter coincides with the November-March season of dust transport [*Pandithurai et al., 2001*], and therefore fire cases were chosen at the onset of the burning season - in November to minimize the dust influence.

Years 2006 and 2007 were those of very little biomass burning in Alaska, so only few cases were observed by MODIS, out of which only four were both large enough to be seen from space and sufficiently un-obscured by clouds to be used for this analysis.

4 Results and discussion

4.1 Comparison of emission options

Emission options defined in section 2.4 provide a range of BB emission estimates. Figure 2a shows total dry mass burned globally in 2006, as estimated by each emission option. Since the QFED inventory calculates aerosol emissions directly from MODIS-measured FRP, it does not provide a DM estimate. Figure 2b illustrates the differences in corresponding 2006 global BB emissions of BC. The comparisons for OC and SO₂ (not shown here) produce similar patterns to that of BC. The magnitudes of SO₂ emissions are similar to those of BC, and OC emissions are approximately eight times larger, as expected from the values of species emission factors introduced in section 2.1.3. Comparisons of both DM and emissions of individual aerosol species for 2007 also show similar patterns.

The differences between individual emission options can be quite large. Thus, the largest estimate of global total BC emissions by the mod1-CCm-GOCART option is about eight times larger than that in GFED3. These differences can be explained by the choice of parameters that were combined according to Equation 1. Some of these differences are briefly discussed below.

Estimates of burned area by MCD45, GFED3, and a version of mod1 were compared in detail in previous studies by *Roy et al.* [2008] and *Giglio et al.* [2010]. Although the total burned areas reported by all three products globally in 2006 are very similar: 3.94×10^6 km² in mod1, 3.96×10^6 km² in MCD45, 3.41×10^6 km² in GFED3, their performance in different ecosystems is noticeably distinct. *Roy, Boschetti et al.* [2008] demonstrated that in ecosystems having low Leaf Area Index (LAI) and low percent tree cover - shrublands, grasslands, and savannas, the active fire product (mod1) estimates less burned area (BA) than MCD45. On the other hand, when the percent tree cover is high, especially evergreen forests - both needleleaf (mostly in boreal regions) and broadleaf (mostly in equatorial regions), mod1 reports more BA compared to MCD45. GFED3 burned area estimates are similar to those from MCD45 in many regions [*Giglio et al.*, 2010]. Croplands are an exception to this pattern, and although having low LAI at the time of burning, more BA is reported globally by mod1 than the MCD45 algorithm for this category [*Roy et al.*, 2008], with GFED3 BA being even lower than MCD45 in croplands [*Giglio et al.*, 2010].

Since most of the area burned is a result of fires in Africa, followed by South America and Australia, BB emissions from vegetation types dominant in these regions (GLC codes 1, 3, and 12) show the largest absolute differences, consistent with the described BA detection patterns. The differences in estimated BA and subsequent emissions can be quite large regionally, such as in boreal regions covered by evergreen needle-leaf forests (GLC code 4), or

in tropical crops and shrubs (GLC code 17), but their contribution to total global emissions is relatively small.

The chosen fuel consumption ($B^*\beta$ in Eq. 1) products have not been explicitly compared elsewhere. Since no static fuel consumption is provided in the GFED3 dataset, we obtained the equivalent fuel consumption by dividing the GFED3 monthly values of burned dry mass by the corresponding value of burned area in every GOCART grid box. Average fuel consumption from all the available data for the period of 1997-2009 is shown in Fig. 3e. The maps of absolute fuel consumption differences emphasize the discrepancies between the datasets, where the largest differences are in the forested boreal and tropical regions. CC estimates of fuel consumption by fires of high severity (CCh) have the largest values, and CCl - the lowest. Assuming all fires of medium fire severity for a reference, we compare the absolute values of fuel consumption in the datasets. The general trend, which shows the CCm dataset including all fires of medium severity (CCm) as giving largest fuel consumption estimates, followed by the GLC and GFED3, is reversed in the boreal needleleaf forest where the GFED3 fuel consumption is the largest, followed by GLC and CCm, and is partially reversed in the parts of tropical forest where GFED3 is the largest, followed by CCm and GLC.

The Haines Index tends to increase the average daily fuel consumption in most regions if it serves as a proxy for fire severity to determine fuel consumption, as described in section 2.1.2.

The GLC and GFED emission factors are similar and are all generally lower than the GOCART standard E_f 's. This difference is smallest in the extra-tropical forest, and is largest in the grasslands and shrublands, where the standard GOCART option can be up to a factor 2 to 3 larger than either the GLC or GFED E_f 's.

4.2 Evaluation of emission options using GOCART and MODIS AOD

We compared GOCART AOD, sampled at the closest time to the satellite overpass from each of 13 model runs, with MODIS AOD averaged to the model grid. The maps of MODIS and GOCART AOD within each case box were visually inspected to evaluate the spatial features of the simulated plume. As an example, Figure 4 shows the MODIS visible image, retrieved MODIS AOD with original 10-km resolution, re-gridded MODIS AOD to model grid, and snapshots of GOCART AOD from all runs with different emission options for case 11 in Russia on July 20, 2006. As noted earlier, QFED dataset uses MODIS AOD as one of the input datasets for estimating emissions, so AOD from QFED-based GOCART runs cannot be fairly compared to MODIS AOD.

To limit analysis of aerosol properties to smoke within the plumes, a threshold AOD value (provided in Table 4) was chosen by visual inspection of MODIS and GOCART AOD maps for each case, with an attempt to separate smoke plumes from the background. The values of all pixels where AOD exceeded the threshold were considered in calculating average AOD values for MODIS observations and model simulations in each case.

Since the bulk of BB aerosol emissions consists of mainly BC and OC [*Andreae and Merlet, 2001; Seinfeld and Pandis, 1998*], BB emissions are represented by the sum of BC and OC emissions in subsequent analysis. The GOCART model works with aerosol emissions in terms of emission rates, expressed in units of mass of aerosol species per unit area per unit time. Therefore, to use satellite AOD as a constraint for BB emissions in the model, we first explore the relationship between emissions input into the model and simulated AOD output. This relationship is plotted in Figure 5. To keep the analysis independent of the fire case box size, we use units of emission rate ($\text{kgC km}^{-2} \text{ day}^{-1}$) to characterize emission amount. The values from all

model runs and all fire cases are colored according to the region where the fire is located. The region colors are defined in Figure 1.

The same dataset, plotted for each region separately, follows in Figure 6. Colors are used here to represent different emission options, and symbols distinguish fire cases occurring in a given region. Symbols corresponding to each fire case are given in Table 4. The symbol associated with the emission option that produces the average GOCART AOD closest to the average MODIS AOD for each case is highlighted in black. Connected to each such symbol is a black line showing the difference between this model average AOD and the MODIS average AOD for this case (i.e., MODIS measurement would plot at the end of this black line).

The regional performance of the model with different emission inventories is presented in Figure 7 in a series of maps, where each map shows the performance of GOCART with BB aerosol estimated by one of the emission options. The color of each case box in Figure 7 shows the ratio of average GOCART AOD to average MODIS AOD. The darker the red color, the more GOCART overestimates MODIS AOD, and the darker the blue color, the lower the GOCART AOD compared to MODIS. Green color marks the cases where GOCART and MODIS average AOD are within about 20% of each other. Figure 7 is further summarized in Table A in the supplementary material to this paper. The major trends highlighted in Figures 5, 6, and 7 follow.

- Data points in Figures 5 and 6 form a pattern of two distinct regimes:
 - In the first regime the points are clustered parallel to the horizontal axis. These are regions dominated by background aerosol, where the BB contribution does not significantly affect the total AOD. This happens, for example, when the BB AOD is very low and is not much higher than AOD of the environment, such as in some cases in the USA. Alternatively, the

background aerosol loading can be so high that even substantial BB emissions do not contribute a dominant fraction to the total AOD. Such are the cases in China and India. Qualitatively, in the areas where AOD is dominated by non-BB aerosols, different BB inventories make little differences in GOCART AOD. In contrast, even though the non-BB background AOD is also rather high in South-East Asia, North-Central Africa, and Central and Eastern Europe, the contribution of BB aerosol is significant enough that the choice of emission inventory measurably affects the total AOD. The contribution to total AOD in the model from different aerosol types was evaluated both spatially and in magnitude to come to this conclusion. Wind dispersal, which also tends to flatten the curves in Figure 6 regardless of background aerosol level, is discussed in Section 4.3 below.

- In the second regime, AOD depends on the amount of smoke emissions. This "BB-dominated" regime appears after a certain amount of emissions has been reached, i.e., after the contribution of BB aerosol to total AOD starts to noticeably overweigh the background aerosol components.

- The spread of the data points along the X-axis in each case in Figure 6 (cases are distinguished by different symbols here) shows the range of estimates provided by different emission options. The spread of values is generally larger, i.e. the discrepancies between emission rates estimated by different inventories are large, in background-dominated areas where the area is polluted (India, China, Eastern Europe), the observed plume is not well-defined or small (some US cases, Alaska), or the event is long-lasting so overlying thick smoke prevents good observations of burned area and fire properties (some cases in Canada, Indonesia). In BB

emission-dominated regions (Russia, North Australia, South America), emission estimates from different emission options are fairly similar, but given a steep slope of the AOD vs. (BC+OC) emissions relationship, even a small change in emission amount has a significant effect on the simulated AOD.

- Qualitative comparison of the GOCART and MODIS AOD maps shows that the model performs better spatially and more consistently in magnitude in the cases having large, distinct biomass burning plumes, such as the case in Russia, shown in Figure 4. Thus, intense fires in the forested areas of Russia, Indonesia and Canada are best modeled by GOCART spatially, and the relative performance of the model is consistent from case to case when different emission inventories are used. These are the regions where the majority of emissions are only from BB sources and the plumes are significantly thick and distinct from the background. These are also regions of dark, densely vegetated surface, the best conditions for MODIS over-land AOD retrieval [*Levy et al.*, 2010].

- Figure 8 shows average MODIS AOD for each case. Examination of this figure together with maps of Figure 7 suggests that in regions having average MODIS AOD 0.5 or larger, the simulated AOD is lower than observed, regardless of the emission option used (except "mod1-CCi-GOCART" option in Russia). These regions include Russia, South Australia, part of Latin America (Honduras), and Indonesia. In the regions with average MODIS AOD values of 0.5 or lower, the GOCART vs. MODIS AOD comparison is less consistent.

- Persistent low bias of GOCART BB AOD in Indonesia, South Australia and Russia merits further investigation, but is immediately related to omissions in biomass burning emission estimates.

- Model underestimation of total AOD in heavily pollution dominated regions of India and China have been shown previously [*Chin et al.*, 2009], a problem that is mostly associated with the anthropogenic and dust emissions and transport.

- Regarding the regional performance of individual emission options:

- The choice of MCD45-based emission options can lead to extreme AOD overestimation in the tropical regions - Africa, Latin America, North Australia, South-East Asia and very low AOD values in the forest regions for Russia, Canada, Indonesia, and South Australia.
- As mentioned above, assuming 1 km² per fire count produces a higher-end estimate of burned area, and the "mod1"-based emission options tend to overestimate emissions, often by large factors in some regions (Latin and South America, Africa), but these high emission estimates bring simulated AOD close to MODIS-observed in the boreal regions.
- The use of GFED emission inventories generally leads to the best AOD comparison in Africa, where other inventories overestimate MODIS AOD, but in most other regions GFED-based model runs have AOD lower than MODIS, more so with monthly (GFEDv2, and GFED3) than daily inventories, as expected. Also as expected, monthly GFED inventories appear to perform well for the long-burning events in the sparsely vegetated regions of Africa, North Australia, South-East Asia, and tend to underestimate emissions more for intense individual fires in Russia, Canada, and the USA.
- Using the GFED3-daily emission inventory does not lead to a consistent improvement in all regions over monthly GFED3 estimates, but, as expected,

it improves performance for shorter-lived fires. However, the larger values of GOCART standard emission factors bring the emission estimates up, and closer to observations.

4.3 Effect of aerosol dispersion on AOD

Spatial distribution of AOD depends not only on the source strength, but also on the rate at which the plume is dissipated. Therefore, to quantitatively evaluate AOD-emissions relationship we have to account for smoke dissipation. Smoke plume dispersion is governed by wind shear and turbulence in the surrounding environment. Thus, strong vertical and horizontal atmospheric motions within the environment promote clear air entrainment, mixing, and plume dispersion. Plumes in stable air tend to stay more confined. Since smoke plume optical depth is proportional to smoke density, it is reasonable to assume that compact and well-contained plumes will be optically thicker than more dispersed plumes containing the same amount of aerosol particles. Therefore, in the BB-dominated regime, we expect similar changes in emission amount to have different effects on the resultant AOD. Further, we investigate the relationship between plume environment, aerosol dispersion and their effects on simulated AOD values.

4.3.1 Height of smoke plumes and vertical dispersion

The vertical structure of the smoke events studied was investigated by visually examining the MISR stereo height of the plumes or CALIPSO profiles whenever these observations were available. Since vertical dispersion of aerosol in the atmospheric column in itself has little effect on total column AOD, we mostly checked whether the smoke was confined to the relatively well-mixed planetary boundary layer (PBL, as defined by GEOS4-DAS). Figure 9 provides an example of how MISR and CALIPSO observations are used to find the plume height. Both instruments passed over the plume in case 11 on the same day as MODIS. It is worth

remembering that CALIPSO-Day measurement was made approximately 2.5 hours after MISR, and CALIPSO-Night observation, spatially coincident with MISR, occurred about 16 hours after MISR and MODIS snapshots. CALIPSO vertical feature mask are overlaid with the GEOS-4 PBL height, which is between about 2 and 3 km above terrain. Both CALIPSO aerosol profiles and histograms of MISR pixel heights indicate aerosol signature within the boundary layer, especially at the source, while detecting some higher clouds around 10 km. MISR heights away from the BB emission sources and CALIPSO-Day measurements have signature of aerosol possibly transported above the PBL. PBL height being considerably lower at night, a height of the mixed layer, approximated by PBL height at 6:30 AM UTC (13:30 local time), is also shown in dashed line in Figure 9 on CALIPSO-Night plot.

If the smoke is injected directly into the free troposphere, the horizontal winds can transport it away fast enough to prevent accumulation of smoke and affect our conclusions about total AOD as a proxy for cumulative strength of BB sources. Although smoke injection above the PBL does occur in some cases [*Kahn et al.*, 2008; *ValMartin et al.*, 2010], except for the few large burning events in Russia, Canada, Indonesia and South Australia studied here (cases 47, 48, 50, 2, 3, 14, 15, 16, 18, 20) where smoke was found in the free troposphere, analysis similar to that shown in Figure 4 suggests it was lifted there after initial injection into the boundary layer, and these cases conform to the general patterns described in the analysis sections below.

4.3.2 Wind speed and horizontal dispersion

To calculate average PBL wind speed for each case we average absolute mid-PBL wind speeds in all model grid boxes where the BB sources are defined. The same data points as in Figure 6 are plotted in Figure 10, now colored by the average PBL wind speed in the case box. A number of factors affect the apparent relationship between the AOD, which reflects the local

concentration of aerosol particles, and the plume emission strength. We expect the AOD to be directly related to the emission strength, and inversely related to the local wind speed, which dissipates the aerosol. So other factors being equal, the slope of the AOD vs. emission strength line would be steeper in cases having lower wind speeds, and shallower when the wind speed is higher. However, the atmospheric stability structure also affects the result, as the aerosol will tend to dissipate more readily in a less stable atmosphere, and if background aerosol dominates the emission source, the ambient AOD might not be significantly affected by changes in the strength of a local source, as discussed in Section 4.2 above.

4.4 Possibility of using MODIS AOD as a quantitative constraint on biomass burning aerosol emissions

To use satellite observation of AOD as a constraint to model emissions, a quantitative relationship must exist between the actual BB emission rate and MODIS-observed AOD, assuming that GOCART model can reproduce this relationship. We have already established that wind speed is an important factor that governs AOD-emissions relationship in BB-dominated regions. Therefore, we find a fit to the data points in the AOD vs. emissions (BC+OC) plots for every region as is described below, and this relationship is the one needed to find the emission rate required to produce observed AOD in the given environmental conditions. GOCART average AOD closest to the MODIS average AOD for each case has been marked with black symbols, as in Figure 6, with a line from each such data point showing the magnitude of AOD under- or overestimation compared to the average MODIS AOD.

In each region, several lines, each corresponding to one of the three wind speed categories (0-3, 3-6, and > 6 m/s) were fitted to the data points in the BB-dominated regime in Figure 10. An empirical emission density cutoff between background-dominated and BB-

dominated regimes was chosen in each region where a BB-dominated regime is observed, and these cutoff values are listed in table 5. The emission rate cutoff value is found to be around 10 kg/km²/day, where stronger emissions are likely to measurably affect the total column AOD, but varying depending on the background AOD. The data suggest that a larger cutoff value is required for India, probably due to a more polluted background, and a lower value in North Australia, for which there are no data clusters parallel to the X-axis to form a background-dominated regime. No emission density cutoff could be selected for Alaska and China due to very faint plumes in the former (in the cases studied here) and a total domination of background aerosol in the latter. The data points falling into three wind speed categories (0-3, 3-6, and > 6 m/s) can be fit to equations of the form (linear fit on a log-log plot):

$$Y = \exp(a) * X^b, \quad [3]$$

where X is the OC+BC daily-integrated fire emission in kg per km², Y is the average GOCART AOD within the plume, and the resulting wind-regime-dependent regional fit coefficients *a* and *b* are listed in Table 5. The quantitative relationship between AOD and aerosol emission rate as a function of wind speed allows the use of MODIS AOD to constrain the BC+OC emission rate in the model, assuming the plume is emitted into the PBL and the average PBL wind speed is known. Such estimates should be more certain under lower wind speed conditions (due to small changes in emissions leading to significant changes in AOD), and less certain under higher wind speed conditions, where a larger range of emission rates is allowed within available constraints.

4.5 Limitations of the method, and topics for further study

Our method of using MODIS AOD to constrain BB emissions in the global model has some limitations:

- The method is based on the assumption that the discrepancies between MODIS and GOCART AOD are predominantly caused by the under- or over-estimate of emissions, such that the errors in aerosol removal or mass extinction efficiency (converting aerosol mass to AOD) are much smaller than that in emissions. This assumption could be wrong in some cases.
- It has been shown that total column AOD provides a poor constraint on BB emissions in background-dominated regions.
- The effect of wind speed on the AOD-emissions relationship has to be explored further in the light of interaction of smoke plume with more or less polluted environment.
- Even though physically sound, the relationship between AOD and BB aerosol emission rate has been quantitatively described for one version of the GOCART model only, and its application to models having different spatial resolution and physical aerosol processes needs to be investigated.
- The use of the MODIS AOD product brings a set of its own limitations, such as missing AOD retrievals in the cores of very optically thick plumes, over bright surfaces, or in regions with complex cloud cover, and AOD over- or underestimation in some situations [*Levy et al.*, 2010]. The notes are provided in table 4 for the regions where AOD retrievals were missing in the studied fire cases. In the cases where MODIS AOD cannot be retrieved, AOD from other satellite instruments can be used when available.
- The results in this study are based on one year of fire observations. Inter-annual variability of fire locations and intensity merits further investigation, to test the

applicability of the method quantitatively in regions where fire seasons, and thus, fire and smoke properties and amount, can vary significantly.

- Since the global model is too coarse to simulate individual smoke plumes of sub-grid size, the method is rendered insensitive to small AOD variations when averaging MODIS AOD, and is similarly insensitive to small aerosol concentration changes, when the model requires an aerosol emission source the size of an entire grid box.

5 Conclusions

We used ready-to-use global biomass burning aerosol emission inventories GFEDv2, GFED3, and QFED, as well as several combinations of burned area, fuel consumption and aerosol emission factor estimates for this study, which resulted in a total of thirteen global BB emission options. We compared the amounts of BB aerosol emitted during the year 2006, as estimated by all thirteen emission options, and found that annual global total BC or OC emission estimates can differ by a factor of eight, with GFED3 providing the lowest estimate, and emission options based on MODIS fire counts, Langley Carbon Consumption estimates and GOCART emission factors producing the largest. Although emission factor and fuel consumption choices can each lead to about a factor of two-to-three difference in a given region, burned area estimates can vary dramatically between the inventories, producing the largest differences between emission options. The performance of these emission options in the GOCART model was evaluated by comparing model simulated AOD to the MODIS-measured AOD. AOD from QFED-based model runs could not be fairly used in such comparison, due to the use of MODIS AOD as one of the parameters in calibrating QFED emissions.

Twelve GOCART runs, each with a different emission option, comprise an ensemble of runs, providing a range of input emissions and output AOD estimates that were evaluated for 124 fire events chosen globally. In general, the model performs best spatially and most consistently in magnitude, when simulating large biomass burning events of Russia and Canada, and less consistently in the regions where other sources of aerosol, such as anthropogenic pollution or dust, make significant contributions to the background - Asia, Africa, Central-Eastern Europe. In regions of complex terrain and patchy vegetation, such as the USA, the inventories do not agree well, and the comparison between GOCART and MODIS is not consistent.

The use of GFED inventories leads to the best AOD agreement in Africa, where other inventories overestimate MODIS AOD, but in most other regions GFED-based runs have lower-than-MODIS AOD. The use of daily GFED emissions generally improves AOD comparison compared to the use of monthly emission estimates in the cases of short-lived individual fires. Emission estimates based on MCD45 burned area lead to significant AOD underestimation in higher latitudes, and overestimation in Africa. 'mod1'-based model runs result in the best AOD comparisons in the boreal regions, while mostly overestimating AOD in the tropical regions.

The relationship between BB aerosol, expressed as a sum of BC and OC emissions, and the resultant AOD, forms two distinct regimes. First is the "BB-dominated" regime where BB is the main aerosol source, and changes in BB emission rate clearly affects the total AOD in the region. Second is the "background-dominated" regime, in which the contribution of BB smoke to the total AOD is small enough that changes in smoke emission rate does not produce significant total-AOD changes. The rate of BC+OC emission from BB (in units of $\text{kg}/\text{km}^2/\text{day}$) needs to be larger than a certain threshold for emission-AOD relationship to be in BB-dominated regime.

This threshold is around $10 \text{ kg/km}^2/\text{day}$ in most regions studied, when the source is of the size of the GOCART model grid box, but varies depending on the background AOD level.

The rate of change of AOD in response to change in amount of BB emissions is affected by the dispersion potential of the plume environment, which is usually dominated by the wind speed and atmospheric stability. In clean environments, higher wind speeds lead to shallower slopes of the AOD vs. emissions relationships, meaning larger changes in AOD are needed to noticeably affect the total column AOD. Thus, given a quantitative relationship between AOD and BB emissions in each geographic region, satellite-measured AOD can be used to constrain the BB source strength, given the average wind speed in the region. However, MODIS total column AOD cannot be used to constrain BB emissions in the background-dominated regime, and the regional quality of the MODIS AOD product also has to be considered when using it as a quantitative constraint.

Acknowledgements

We thank Catherine Liousse for providing GLC2000 fuel consumption files and emission factors, Anton Darmanov and Arlindo da Silva for providing access to QFED emission dataset, Matthew Davis and James Limbacher for software support when processing satellite data products, and Thomas Diehl and Qian Tan for help with configuring the GOCART model. This work was funded primarily by NASA grants NNX08AU81H and NNX10AG61G to Purdue University. The work of R. Kahn is supported in part by NASA's Atmospheric Composition Program, and NASA's Climate and Radiation Research and Analysis Program under H. Maring.

References:

- Akagi, S. K., R. J. Yokelson, C. Wiedinmyer, M. J. Alvarado, J. S. Reid, T. Karl, J. D. Crounse, and P. O. Wennberg (2011), Emission factors for open and domestic biomass burning for use in atmospheric models, *Atmospheric Chemistry and Physics*, *11*, 4039-4072.
- Al-Saadi, J., A. Soja, R. B. Pierce, J. Szykman, C. Wiedinmyer, L. Emmons, S. Kondragunta, X. Zhang, C. Kittaka, T. Schaack, and K. Bowman (2008), Intercomparison of near-real-time biomass burning emissions estimates constrained by satellite fire data, *Journal of Applied Remote Sensing*, *2*(021504).
- Alexeyev, V. A., and R. A. Birdsey (1998), Carbon storage in forests and peatlands of Russia *Rep.*, USDA, Forest Service, Northeast Research Station, Radnor, PA.
- Andreae, M. O., and P. Merlet (2001), Emission of trace gases and aerosols from biomass burning, *Global Biogeochemical Cycles*, *15*(4), 955-966.
- Bartholome', E., and A. S. Belward (2005), GLC2000: a new approach to global land cover mapping from Earth observation data, *International Journal of Remote Sensing*, *26*(9), 1959–1977.
- Bäumer, D., B. Vogelb, S. Versickb, R. Rinkeb, O. Möhlerb, and M. Schnaiter (2008), Relationship of visibility, aerosol optical thickness and aerosol size distribution in an ageing air mass over South-West Germany *Atmospheric Environment*, *42*(5), 989-998.
- Bloom, S., A. d. Silva, D. Dee, M. Bosilovich, J.-D. Chern, S. Pawson, S. Schubert, M. Sienkiewicz, I. Stajner, W.-W. Tan, and M.-L. Wu (2005), Documentation and validation of the Goddard Earth Observing System (GEOS) data assimilation system - version 4 *Rep.*, NASA Goddard Space Flight Center, Greenbelt, MD.

725 Boucher, O., and T. L. Anderson (1995), General circulation model assessment of the sensitivity
 726 of direct climate forcing by anthropogenic sulfate aerosols to aerosol size and chemistry,
 727 *Journal of Geophysical Research*, *100*(D12), 26,117-126,134.

728 CCSP (2009), Atmospheric aerosol properties and climate impacts, a report by the U.S. Climate
 729 Change Science Program and the subcommittee on global change research *Rep.*, National
 730 Aeronautics and Space Administration, D.C., USA.

731 Chin, M., T. Diehl, P. Ginoux, and W. Malm (2007), Intercontinental transport of pollution and
 732 dust aerosols: implications for regional air quality, *Atmospheric Chemistry and Physics*, *7*,
 733 5501-5517.

734 Chin, M., R. B. Rood, S.-J. Lin, J.-F. Muller, and A. M. Thompson (2000), Atmospheric sulfur
 735 cycle simulated in the global model GOCART: Model description and global properties.,
 736 *Journal of Geophysical Research*, *105*(D20), 24,671-624,687.

737 Chin, M., T. Diehl, O. Dubovik, T. F. Eck, B. N. Holben, A. Sinyuk, and D. G. Streets (2009),
 738 Light absorption by pollution, dust, and biomass burning aerosols: a global model study and
 739 evaluation with AERONET measurements, *Annales Geophysicae*, *27*, 3439–3464.

740 Chin, M., P. Ginoux, S. Kinne, O. Torres, B. N. Holben, B. N. Duncan, R. V. Martin, J. A.
 741 Logan, A. Higurashi, and T. Nakajima (2002), Tropospheric aerosol optical thickness from
 742 the GOCART model and comparisons with satellite and sun photometer measurements,
 743 *Journal of the Atmospheric Sciences*, *59*, 461-483.

744 Choi, Y., S. A. Vay, K. P. Vadrevu, A. J. Soja, J.-H. Woo, S. R. Nolf, G. W. Sachse, G. S.
 745 Diskin, D. R. Blake, N. J. Blake, H. B. Singh, M. A. Avery, A. Fried, L. Pfister, and H. E.
 746 Fuelberg (2008), Characteristics of the atmospheric CO₂ signal as observed over the

747 conterminous United States during INTEx-NA, *Journal of Geophysical Research*,
748 113(D07301), doi:10.1029/2007JD008899.

749 Colarco, P. R., M. R. Schoeberl, B. G. Doddridge, L. T. Marufu, O. Torres, and E. J. Welton
750 (2004), Transport of smoke from Canadian forest fires to the surface near Washington, D.C.:
751 Injection height, entrainment, and optical properties, *Journal of Geophysical Research*,
752 109(D06203), doi:10.1029/2003JD004248.

753 Damoah, R., N. Spichtinger, C. Forster, P. James, I. Mattis, U. Wandinger, S. Beirle, T. Wagner,
754 and A. Stohl (2004), Around the world in 17 days – hemispheric-scale transport of forest fire
755 smoke from Russia in May 2003, *Atmospheric Chemistry and Physics*, 4, 1311–1321.

756 Dentener, F., D. Stevenson, J. Cofala, R. Mechler, M. Amann, P. Bergamaschi, F. Raes, and R.
757 Derwent (2005), The impact of air pollutant and methane emission controls on tropospheric
758 ozone and radiative forcing: CTM calculations for the period 1990–2030, *Atmospheric*
759 *Chemistry and Physics*, 5, 1731–1755.

760 Dentener, F., S. Kinne, T. Bond, O. Boucher, J. Cofala, S. Generoso, P. Ginoux, S. Gong, J. J.
761 Hoelzemann, A. Ito, L. Marelli, J. E. Penner, J.-P. Putaud, C. Textor, M. Schulz, G. R. v. d.
762 Werf, and J. Wilson (2006), Emissions of primary aerosol and precursor gases in the years
763 2000 and 1750 prescribed data-sets for AeroCom, *Atmospheric Chemistry and Physics*, 6,
764 4321–4344.

765 Dey, S., and L. Di Girolamo (2010), A climatology of aerosol optical and microphysical
766 properties over the Indian subcontinent from 9 years (2000–2008) of Multiangle Imaging
767 Spectroradiometer (MISR) data, *Journal of Geophysical Research*, 115(D15204),
768 doi:10.1029/2009JD013395.

769 Diner, D. J., J. C. Beckert, T. H. Reilly, C. J. Bruegge, J. E. Conel, R. A. Kahn, J. V. Martonchik,
 770 T. P. Ackerman, R. Davies, S. A. W. Gerstl, H. R. Gordon, J.-P. Muller, R. B. Myneni, P. J.
 771 Sellers, B. Pinty, and M. M. Verstraete (1998), Multi-angle Imaging SpectroRadiometer
 772 (MISR) instrument description and experiment overview, *IEEE Transactions on Geoscience*
 773 *and Remote Sensing*, *36*(4), 1072-1087.

774 Dubovik, O., T. Lapyonok, Y. J. Kaufman, M. Chin, P. Ginoux, R. A. Kahn, and A. Sinyuk
 775 (2008), Retrieving global aerosol sources from satellites using inverse modeling,
 776 *Atmospheric Chemistry and Physics*, *8*, 209-250.

777 Duncan, B. N., R. V. Martin, A. C. Staudt, R. Yevich, and J. Logan (2003), Interannual and
 778 seasonal variability of biomass burning emissions constrained by satellite observations,
 779 *Journal of Geophysical Research*, *108*(D2), doi:10.1029/2002JD002378.

780 EOSDIS (2009), Earth Observing System Data and Information System (EOSDIS), Earth
 781 Observing System ClearingHouse (ECHO) / Warehouse Inventory Search Tool (WIST)
 782 version 10.X [online application], edited, EOSDIS, Goddard Space Flight Center (GSFC)
 783 National Aeronautics and Space Administration (NASA), Greenbelt, MD.

784 Fritz, S., and L. See (2008), Identifying and quantifying uncertainty and spatial disagreement in
 785 the comparison of global land cover for different applications, *Global Change Biology*, *14*,
 786 1057–1075, doi: 10.1111/j.1365-2486.2007.01519.x.

787 Giglio, L. (2010), MODIS collection 5 active fire product user's guide version 2.4 *Rep.*, NASA
 788 Goddard Space Flight Center, Greenbelt, MD.

789 Giglio, L., I. Csizsar, and C. O. Justice (2006a), Global distribution and seasonality of active
 790 fires as observed with the Terra and Aqua Moderate Resolution Imaging Spectroradiometer

791 (MODIS) sensors, *Journal of Geophysical Research*, 111(G02016),
 792 doi:10.1029/2005JG000142.

793 Giglio, L., G. R. van der Werf, J. T. Randerson, G. J. Collatz, and P. Kasibhatla (2006b), Global
 794 estimation of burned area using MODIS active fire observations, *Atmospheric Chemistry and*
 795 *Physics*, 6, 957-974.

796 Giglio, L., T. Loboda, D. P. Roy, B. Quayle, and C. O. Justice (2009), An active-fire based
 797 burned area mapping algorithm for the MODIS sensor, *Remote Sensing Environment*, 113,
 798 408-420.

799 Giglio, L., J. T. Randerson, G. R. v. derWerf, P. S. Kasibhatla, G. J. Collatz, D. C. Morton, and
 800 R. S. DeFries (2010), Assessing variability and long-term trends in burned area by merging
 801 multiple satellite fire products, *Biogeosciences*, 7, 1171-1186.

802 Ginoux, P., M. Chin, I. Tegen, J. M. Prospero, B. Holben, O. Dubovik, and S.-J. Lin (2001),
 803 Sources and distributions of dust aerosols simulated with the GOCART model, *Journal of*
 804 *Geophysical Research*, 106(D17), 20255-20274

805 Gonsamo, A., and J. M. Chen (2011), Evaluation of the GLC2000 and NALC2005 land cover
 806 products for LAI retrieval over Canada, *Canadian Journal of Remote Sensing*, 37(3), 302-
 807 313.

808 Haines, D. A. (1988), A lower atmosphere severity index for wildland fires, *National Weather*
 809 *Digest*, 13, 23-27.

810 Hyer, E. J., and J. S. Reid (2009), Baseline uncertainties in biomass burning emission models
 811 resulting from spatial error in satellite active fire location data, *Geophysical Research*
 812 *Letters*, 36(L05802), doi:10.1029/2008GL036767.

813 Ichoku, C., and Y. Kaufman (2005), A method to derive smoke emission rates from MODIS fire
 814 radiative energy measurements, *IEEE Transactions on Geoscience and Remote Sensing*,
 815 *43*(11), 2636-2649.

816 IPCC (2007), Climate change 2007: the physical science basis. Contribution of working group I
 817 to the fourth assessment report of the intergovernmental panel on climate change *Rep.*, 996
 818 pp. pp, Cambridge, United Kingdom and New York, NY, USA.

819 Ito, A., and J. E. Penner (2004), Global estimates of biomass burning emissions based on satellite
 820 imagery for the year 2000, *Journal of Geophysical Research*, *109*(D14S05),
 821 doi:10.1029/2003JD004423.

822 Jaffe, D., I. Bertsch, L. Jaeglé, P. Novelli, J. S. Reid, H. Tanimoto, R. Vingarzan, and D. L.
 823 Westphal (2004), Long-range transport of Siberian biomass burning emissions and impact on
 824 surface ozone in western North America, *Geophysical Research Letters*, *31*(L16106),
 825 doi:10.1029/2004GL020093.

826 Kahn, R. A., Y. Chen, D. L. Nelson, F.-Y. Leung, Q. Li, D. J. Diner, and J. A. Logan (2008),
 827 Wildfire smoke injection heights: Two perspectives from space, *Geophysical Research*
 828 *Letters*, *35*(L04809), doi:10.1029/2007GL032165.

829 Kahn, R. A., B. J. Gaitley, M. J. Garay, D. J. Diner, T. F. Eck, A. Smirnov, and B. N. Holben
 830 (2010), Multiangle Imaging SpectroRadiometer global aerosol product assessment by
 831 comparison with the Aerosol Robotic Network, *Journal of Geophysical Research*,
 832 *115*(D23209), doi:10.1029/2010JD014601.

833 Kaiser, J. W., A. Heil, M. O. Andreae, A. Benedetti, N. Chubarova, L. Jones, J.-J. Morcrette, M.
 834 Razinger, M. G. Schultz, M. Suttie, and G. R. v. d. Werf (2012), Biomass burning emissions

835 estimated with a global fire assimilation system based on observed fire radiative power,
836 *Biogeosciences*, *9*, 527–554.

837 Kaufman, Y., L. Remer, R. Ottmar, D. Ward, L. Rong-R, R. Kleidman, R. Fraser, L. Flynn, D.
838 McDougal, and G. Shelton (1996), Relationship between remotely sensed fire intensity and
839 rate of emission of smoke: SCAR-C experiment, in *Global Biomass Burning*, edited by J.
840 Levine, pp. 685– 696, MIT Press, Mass.

841 Levy, R. C., L. A. Remer, and O. Dubovik (2007), Global aerosol optical properties and
842 application to Moderate Resolution Imaging Spectroradiometer aerosol retrieval over land,
843 *Journal of Geophysical Research*, *112*(D13210), doi:10.1029/2006JD007815.

844 Levy, R. C., L. A. Remer, R. G. Kleidman, S. Mattoo, C. Ichoku, R. Kahn, and T. F. Eck (2010),
845 Global evaluation of the Collection 5 MODIS dark-target aerosol products over land,
846 *Atmospheric Chemistry and Physics*, *10*, 10399–10420.

847 Liousse, C., M. O. Andreae, P. Artaxo, P. Barbosa, H. Cachier, J. M. Gregoire, P. Hobbs, D.
848 Lavoue, F. Mouillot, J. Penner, M. Scholes, and M. G. Schultz (2003), Deriving global
849 quantitative estimates for spatial and temporal distributions of biomass burning emissions, in
850 *IGAC book on emissions*, edited by C. Granier, P. Artaxo and C. Reeves, Kluwer.

851 Liousse, C., B. Guillaume, J. M. Grégoire, M. Mallet, C. Galy, V. Pont, A. Akpo, M. Bedou, P.
852 Castéra, L. Dungall, E. Gardrat, C. Granier, A. Konaré, F. Malavelle, A. Mariscal, A.
853 Mieville, R. Rosset, D. Sercia, F. Solmon, F. Tummon, E. Assamoi, V. Yoboué, and P. V.
854 Velthoven (2010), Updated African biomass burning emission inventories in the framework
855 of the AMMA-IDAF program, with an evaluation of combustion aerosols, *Atmospheric*
856 *Chemistry and Physics*, *10*, 9631–9646.

857 Lohmann, U., and J. Feichter (2005), Global indirect aerosol effects: a review, *Atmospheric*
858 *Chemistry and Physics*, *5*, 715-737.

859 Mazurek, M., M. C. Masonjones, H. D. Masonjones, L. G. Salmon, G. R. Cass, K. A. Hallock,
860 and M. Leach (1997), Visibility-reducing organic aerosols in the vicinity of Grand Canyon
861 National Park: Properties observed by high resolution gas chromatography, *Journal of*
862 *Geophysical Research*, *102*(D3), 3779-3793.

863 Michel, C., C. Liousse, J.-M. Grégoire, K. Tansey, G. R. Carmichael, and J.-H. Woo. (2005),
864 Biomass burning emission inventory from burnt area data given by the SPOT-
865 VEGETATION system in the frame of TRACE-P and ACE-Asia campaigns, *Journal of*
866 *Geophysical Research*, *110*(D09304), doi:10.1029/2004JD005461.

867 Moroney, C., R. Davies, and J.-P. Muller (2002), Operational retrieval of cloud-top heights using
868 MISR data, *IEEE Transactions on Geoscience and Remote Sensing*, *40*(7), 1532-1540.

869 Mu, M., J. T. Randerson, G. R. v. d. Werf, L. Giglio, P. Kasibhatla, D. Morton, G. J. Collatz, R.
870 S. DeFries, E. J. Hyer, E. M. Prins, D. W. T. Griffith, D. Wunch, G. C. Toon, V. Sherlock,
871 and P. O. Wennberg (2011), Daily and hourly variability in global fire emissions and
872 consequences for atmospheric model predictions of carbon monoxide, *Journal of*
873 *Geophysical Research-Atmospheres*, *116*(D24303), doi:10.1029/2011JD016245.

874 NARSTO (2003), Particulate matter science for policy makers - a NARSTO assessment *Rep.*,
875 510 pp, NARSTO management office (Envair), Pasco, WA.

876 Olson, J. S., R. M. Garrels, R. A. Berner, T. V. Armentano, M. I. Dyer, and D. H. Taalon (1985),
877 The natural carbon cycle, in *Atmospheric Carbon Dioxide and the Global Carbon Cycle.*,
878 edited by J. R. Trabalka, pp. 175-213, US Department of Energy, Washington, DC.

879 Pandithurai, G., R. T. Pinker, O. Dubovik, B. N. Holben, and T. O. Aro (2001), Remote sensing
 880 of aerosol optical characteristics in sub-Sahel, West Africa, *Journal of Geophysical*
 881 *Research*, *106*(D22), 28,347-328,356.

882 Pierce, R. B., T. Schaack, J. A. Al-Saadi, T. D. Fairlie, C. Kittaka, G. Lingenfelser, M.
 883 Natarajan, J. Olson, A. Soja, T. Zapotocny, A. Lenzen, J. Stobie, D. Johnson, M. A. Avery,
 884 G. W. Sachse, A. Thompson, R. Cohen, J. E. Dibb, J. Crawford, D. Rault, R. Martin, J.
 885 Szykman, and J. Fishman (2007), Chemical data assimilation estimates of continental U.S.
 886 ozone and nitrogen budgets during the Intercontinental Chemical Transport Experiment—
 887 North America, *Journal of Geophysical Research*, *112*(D12S21),
 888 doi:10.1029/2006JD007722.

889 Quinn, P. K., T. S. Bates, E. Baum, N. Doubleday, A. M. Fiore, M. Flanner, A. Fridlind, T. J.
 890 Garrett, D. Koch, S. Menon, D. Shindell, A. Stohl, and S. G. Warren (2008), Short-lived
 891 pollutants in the Arctic: their climate impact and possible mitigation strategies, *Atmospheric*
 892 *Chemistry and Physics*, *8*, 1723–1735.

893 Reid, J. S., E. J. Hyer, E. M. Prins, D. L. Westphal, J. Zhang, J. Wang, S. A. Christopher, C. A.
 894 Curtis, C. C. Schmidt, D. P. Eleuterio, K. A. Richardson, and J. P. Hoffman (2009), Global
 895 monitoring and rorecasting of biomass-burning smoke: Description of and lessons from the
 896 Fire Locating and Modeling of Burning Emissions (FLAMBE) program, *IEEE Journal of*
 897 *Selected Topics in Applied Earth Observations and Remote Sensing*, *2*(3), 144-162.

898 Remer, L. A., D. Tanré, Y. J. Kaufman, R. Levy, and S. Mattoo (2006), Algorithm for remote
 899 sensing of tropospheric aerosol from MODIS: Collection 5. Product ID: MOD04/MYD04,
 900 edited, NASA Goddard Space Flight Center, Greenbelt, MD.

901 Rienecker, M. M., M. J. Suarez, R. Todling, J. Bacmeister, L. Takacs, H.-C. Liu, W. Gu, M.
 902 Sienkiewicz, R. D. Koster, R. Gelaro, I. Stajner, and J. E. Nielsen (2008), The GEOS-5 Data
 903 Assimilation System—Documentation of versions 5.0.1, 5.1.0, and 5.2.0 *Rep.*, NASA
 904 Goddard Space Flight Center, Greenbelt, Maryland.

905 Roy, D. P., L. Boschetti, C. O. Justice, and J. Ju (2008), The collection 5 MODIS burned area
 906 product — global evaluation by comparison with the MODIS active fire product, *Remote*
 907 *Sensing Environment*, *112*, 3690-3707.

908 Sapkota, A., J. M. Symons, J. Kleissl, L. Wang, M. B. Parlange, J. Ondov, P. N. Breysse, G. B.
 909 Diette, P. A. Eggleston, and T. J. Buckley (2005), Impact of the 2002 Canadian forest fires
 910 on particulate matter air quality in Baltimore city, *Environmental Science and Technology*,
 911 *39*, 24-32.

912 Schroeder, W., I. Csiszar, L. Giglio, and C. C. Schmidt (2010), On the use of fire radiative
 913 power, area, and temperature estimates to characterize biomass burning via moderate to
 914 coarse spatial resolution remote sensing data in the Brazilian Amazon, *Journal of*
 915 *Geophysical Research*, *115*(D21121), doi:10.1029/2009JD013769.

916 Schultz, M. G., A. Heil, J. J. Hoelzemann, A. Spessa, K. Thonicke, J. Goldammer, A. C. Held,
 917 and J. M. Pereira (2008), Global emissions from wildland fires from 1960 to 2000, *Global*
 918 *Biogeochemical Cycles*, *22*(GB2002), doi:10.1029/2007GB003031.

919 Seaton, A., D. Godden, W. MacNee, and K. Donaldson (1995), Particulate air pollution and
 920 acute health effects, *The Lancet*, *345*(8943), 176-178.

921 See, L. M., and S. Fritz (2006), A method to compare and improve land cover datasets:
 922 Application to the GLC-2000 and MODIS land cover products, *IEEE Transactions on*
 923 *Geoscience and Remote Sensing*, *44*(7), 1740-1746.

924 Seiler, W., and P. J. Crutzen (1980), Estimates of gross and net fluxes of carbon between the
 925 biosphere and the atmosphere from biomass burning, *Climatic Change*, *2*, 207-247.
 926 Seinfeld, J. H., and S. N. Pandis (1998), *Atmospheric chemistry and physics*, John Wiley and
 927 Sons, Inc.
 928 Shindell, D., J.-F. Lamarque, N. Unger, D. Koch, G. Faluveg, S. Bauer, and H. Teich (2008),
 929 Climate forcing and air quality change due to regional emissions reductions by economic
 930 sector, *Atmospheric Chemistry and Physics* *8*, 7101–7113.
 931 Soja, A. J., W. R. Cofer, H. H. Shugart, A. I. Sukhinin, P. W. Stackhouse Jr., D. J. McRae, and
 932 S. G. Conard (2004), Estimating fire emissions and disparities in boreal Siberia (1998-2002),
 933 *Journal of Geophysical Research*, *109*(D14S06), doi:10.1029/2004JD004570.
 934 Soja, A. J., J. Al-Saadi, L. Giglio, D. Randall, C. Kittaka, G. Pouliot, J. J. Kordzi, S. Raffuse, T.
 935 G. Pace, T. E. Pierce, T. Moore, B. Roy, R. B. Pierce, and J. J. Szykman (2009), Assessing
 936 satellite-based fire data for use in the National Emissions Inventory, *Journal of Applied*
 937 *Remote Sensing*, *3*(031504).
 938 Turquety, S., J. A. Logan, D. J. Jacob, R. C. Hudman, F. Y. Leung, C. L. Heald, R. M. Yantosca,
 939 S. Wu, L. K. Emmons, D. P. Edwards, and G. W. Sachse (2007), Inventory of boreal fire
 940 emissions for North America in 2004: Importance of peat burning and pyroconvective
 941 injection, *Journal of Geophysical Research*, *112*(D12S03), doi:10.1029/2006JD007281.
 942 ValMartin, M., J. A. Logan, R. A. Kahn, F.-Y. Leung, D. L. Nelson, and D. J. Diner (2010),
 943 Smoke injection heights from fires in North America: analysis of 5 years of satellite
 944 observations, *Atmospheric Chemistry and Physics*, *10*, 1491–1510.

945 Van der Werf, G. R., J. T. Randerson, L. Giglio, G. J. Collatz, and P. S. Kasibhatla (2006),
 946 Interannual variability in global biomass burning emission from 1997 to 2004, *Atmospheric*
 947 *Chemistry and Physics*, *6*, 3423-3441.

948 Van der Werf, G. R., J. T. Randerson, L. Giglio, G. J. Collatz, M. Mu, P. S. Kasibhatla, D. C.
 949 Morton, R. S. DeFries, Y. Jin, and T. T. v. Leeuwen (2010), Global fire emissions and the
 950 contribution of deforestation, savanna, forest, agricultural, and peat fires (1997-2009),
 951 *Atmospheric Chemistry and Physics*, *10*, 11707–11735.

952 Vaughan, M., S. Young, D. Winker, K. Powell, A. Omar, Z. Liu, Y. Hu and C. Hostetler (2004).
 953 Fully automated analysis of space-based lidar data: an overview of the CALIPSO retrieval
 954 algorithms and data products. SPIE, Bellingham, WA, SPIE.

955 Vermote, E., E. Ellicott, O. Dubovik, T. Lapyonok, M. Chin, L. Giglio, and G. J. Roberts (2009),
 956 An approach to estimate global biomass burning emissions of organic and black carbon from
 957 MODIS fire radiative power, *Journal of Geophysical Research*, *114*(D18205),
 958 doi:10.1029/2008JD011188.

959 Warneke, C., R. Bahreini, J. Brioude, C. A. Brock, J. A. de Gouw, D. W. Fahey, K. D. Froyd, J.
 960 S. Holloway, A. Middlebrook, L. Miller, S. Montzka, D. M. Murphy, J. Peischl, T. B.
 961 Ryerson, J. P. Schwarz, J. R. Spackman, and P. Veres (2009), Biomass burning in Siberia
 962 and Kazakhstan as an important source for haze over the Alaskan Arctic in April 2008,
 963 *Geophysical Research Letters*, *36*(L02813), doi:10.1029/2008GL036194.

964 Werth, P., and R. Ochoa (1993), The evaluation of Idaho wildfire growth using the Haines index,
 965 *Weather and Forecasting*, *8*, 223-234.

966 Wiedinmyer, C., S. K. Akagi, R. J. Yokelson, L. K. Emmons, J. A. Al-Saadi, J. J. Orlando, and
 967 A. J. Soja (2011), The Fire INventory from NCAR (FINN): a high resolution global model to
 968 estimate the emissions from open burning, *Geoscientific Model Development*, *4*, 625–641.

969 Wiedinmyer, C., B. Quayle, C. Geron, A. Belote, D. McKenzie, X. Zhang, S. O'Neill, and K. K.
 970 Wynne (2006), Estimating emissions from fires in North America for air quality modeling,
 971 *Atmospheric Environment*, *40*, 3419–3432.

972 Winker, D. M., M. A. Vaughan, A. Omar, Y. Hu, K. A. Powell, Z. Liu, W. H. Hunt, and S. A.
 973 Young (2009), Overview of the CALIPSO mission and CALIOP data processing algorithms,
 974 *Journal of Atmospheric and Oceanic Technology*, *26*, 2310–2323,doi:
 975 2310.1175/2009JTECHA1281.2311.

976 Winkler, J. A., B. E. Potter, D. F. Wilhelm, R. P. Shadbolt, K. Piromsopa, and X. Bian (2007),
 977 Climatological and statistical characteristics of the Haines Index for North America,
 978 *International Journal of Wildland Fire*, *16*, 139-152.

979 Wooster, M. J. (2002), Small-scale experimental testing of fire radiative energy for quantifying
 980 mass combusted in natural vegetation fires, *Geophysical Research Letters*, *29*(21,2027),
 981 doi:10.1029/2002GL015487.

982 Wooster, M. J., G. Roberts, G. L. W. Perry, and Y. J. Kaufman (2005), Retrieval of biomass
 983 combustion rates and totals from fire radiative power observations: FRP derivation and
 984 calibration relationships between biomass consumption and fire radiative energy release,
 985 *Journal of Geophysical Research*, *110*(D24311), doi:10.1029/2005JD006318.

986 Xiao-Peng, S., H. Chengquan, J. O. Sexton, F. Min, R. Narasimhan, S. Channan, and J. R.
 987 Townshend (2011), An assessment of global forest cover maps using regional higher-

988 resolution reference data sets, paper presented at Geoscience and Remote Sensing
989 Symposium (IGARSS), 2011 IEEE International, 24-29 July 2011.

990 Yu, H., Y. J. Kaufman, M. Chin, G. Feingold, L. A. Remer, T. L. Anderson, Y. Balkanski, N.
991 Bellouin, O. Boucher, S. Christopher, P. DeCola, R. Kahn, D. Koch, N. Loeb, M. S. Reddy,
992 M. Schulz, T. Takemura, and M. Zhou (2006), A review of measurement-based assessments
993 of the aerosol direct radiative effect and forcing, *Atmospheric Chemistry and Physics*, *6*, 613-
994 666.

995 Zinke, P. J., A. G. Stangenberger, W. M. Post, W. R. Emanuel, and J. S. Olson (1986),
996 Worldwide organic soil carbon and nitrogen data *Rep.*, Oak Ridge National Laboratory, Oak
997 Ridge, Tennessee.

998

999

1000 Figure captions:

1001 Figure 1. The 124 fire cases used in this study, with case boxes color-coded by geographic
1002 region. Underlying colors represent the GLC vegetation types described in section 2.1.2.

1003 Figure 2. Left graph (a): Total dry mass burned globally in 2006, reported by GOCART emission
1004 input options considered in this study; Right graph (b): total global emission of BC, each
1005 column representing one emission option. Colors in each bar correspond to dry mass burned
1006 (left) or BC emissions (right) from the GLC vegetation categories outlined in Fig.1.

1007 Figure 3. Fuel consumption estimates in kg/m^2 , by the Carbon Consumption (CC) inventory for
1008 low (a), medium (b) and high (c) fire severity, GLC (d), and GFED3 (e) datasets. Absolute
1009 differences between CCm, GLC, and GFED3 fuel load are in (f), (g), and (h).

1010 Figure 4. Case 11: Russia, 20 July 2006. Top Row: Terra-MODIS visible image of the scene
1011 with fire locations marked in red; total column MODIS AOD with original 10-km resolution,
1012 as provided by MOD04 data product; MODIS total TOA AOD averaged to GOCART grid;
1013 followed by maps of the temporally closest 3-hour output of instantaneous GOCART AOD
1014 values for different emission options. Emission options used as input to each of the model
1015 runs are labeled on top of the corresponding maps.

1016 Figure 5. Average GOCART AOD for each fire case and each model run plotted against average
1017 emission rate for the corresponding case in the corresponding emission option. Data points
1018 are colored by geographic region, with colors defined in Fig. 1.

1019 Figure 6. GOCART AOD vs. average BC+OC emission rate. Different symbols distinguish
1020 individual fire cases. Colors represent different emission options in GOCART. The output of
1021 GOCART run for which the simulated AOD is closest to MODIS is marked in black. The

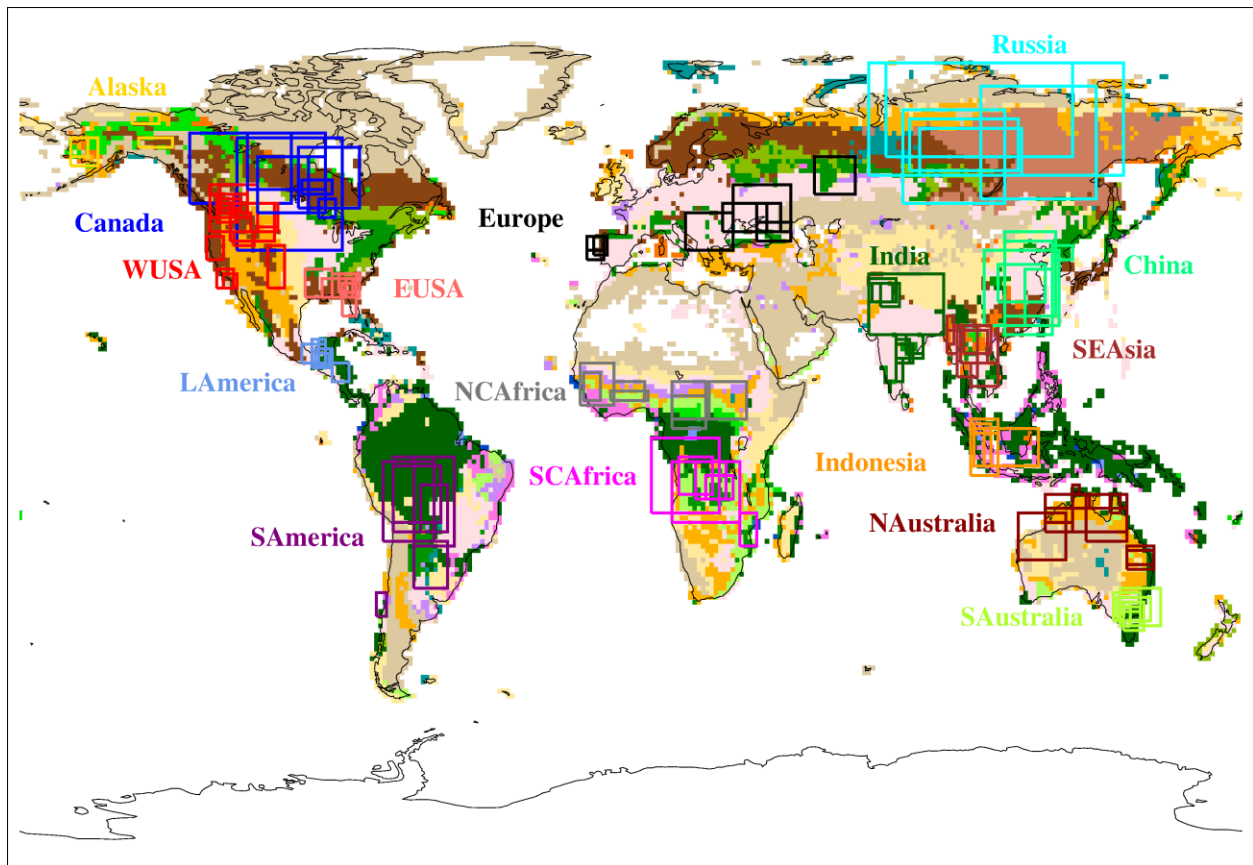
1022 black line from each such data point shows the magnitude of AOD under- or overestimation
1023 compared to the average MODIS AOD.

1024 Figure 7. Ratios of GOCART average AOD to MODIS average AOD for each of the 124 studied
1025 cases, with different emission options used as input to GOCART.

1026 Figure 8. Average MODIS AOD for each of 124 analyzed fire cases.

1027 Figure 9. Case 11: Russia, 20 July 2006. Top Row: Terra-MODIS visible image of the scene
1028 with fire locations marked in red; schematic tracks of CALIPSO and MISR tracks during the
1029 same day in orange and light green, respectively. Satellites are moving in the direction
1030 marked with the errors parallel to the orbits. Map of MISR Stereo heights, and the histograms
1031 of the pixel heights in two regions A (source region) and B (transported aerosol downwind)
1032 are shown in the upper panel. Lower panel shows CALIPSO Vertical feature mask overlaid
1033 by the GEOS-4 PBL height for the coordinates of the case box at the time of CALIPSO
1034 overpass. CALIPSO-Night observation also shows in dashed line the height of the mixing
1035 layer, approximated as the PBL height at 6:30 UTC (13:30 local time).

1036 Figure 10. Same as Fig.6 but here the colors represent average PBL wind speed for each case at
1037 the BB source; the GOCART output closest to MODIS is marked in black.



- | | |
|---|--|
| 1 Tree cover, broadleaved, evergreen | 10 Undefined |
| 2 Tree cover, broadleaved, deciduous, closed | 11 Shrub cover, closed-open, evergreen |
| 3 Tree cover, broadleaved, open | 12 Shrub cover, closed-open, deciduous |
| 4 Tree cover, needle-leaved, evergreen | 13 Herbaceous cover, closed-open |
| 5 Tree cover, needle-leaved, deciduous | 14 Sparse herbaceous or sparse shrub cover |
| 6 Tree cover mixed leaf type | 15 Regularly flooded shrub and/or herbaceous cover |
| 7 Tree cover, regularly flooded, fresh water | 16 Cultivated and managed areas |
| 8 Tree cover, regularly flooded, saline water | 17 Mosaic: Cropland/Tree cover/other natural veg |
| 9 Mosaic: tree cover / other natural vegetation | 18 Cropland/Shrub and/or grass cover |

Figure 1

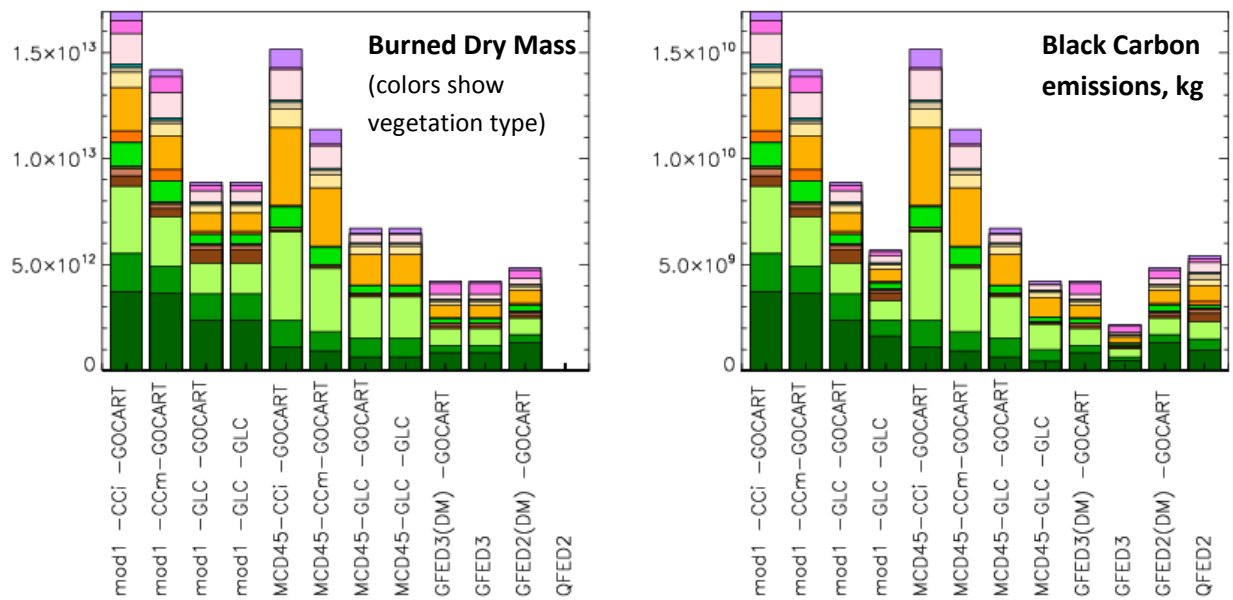


Figure 2

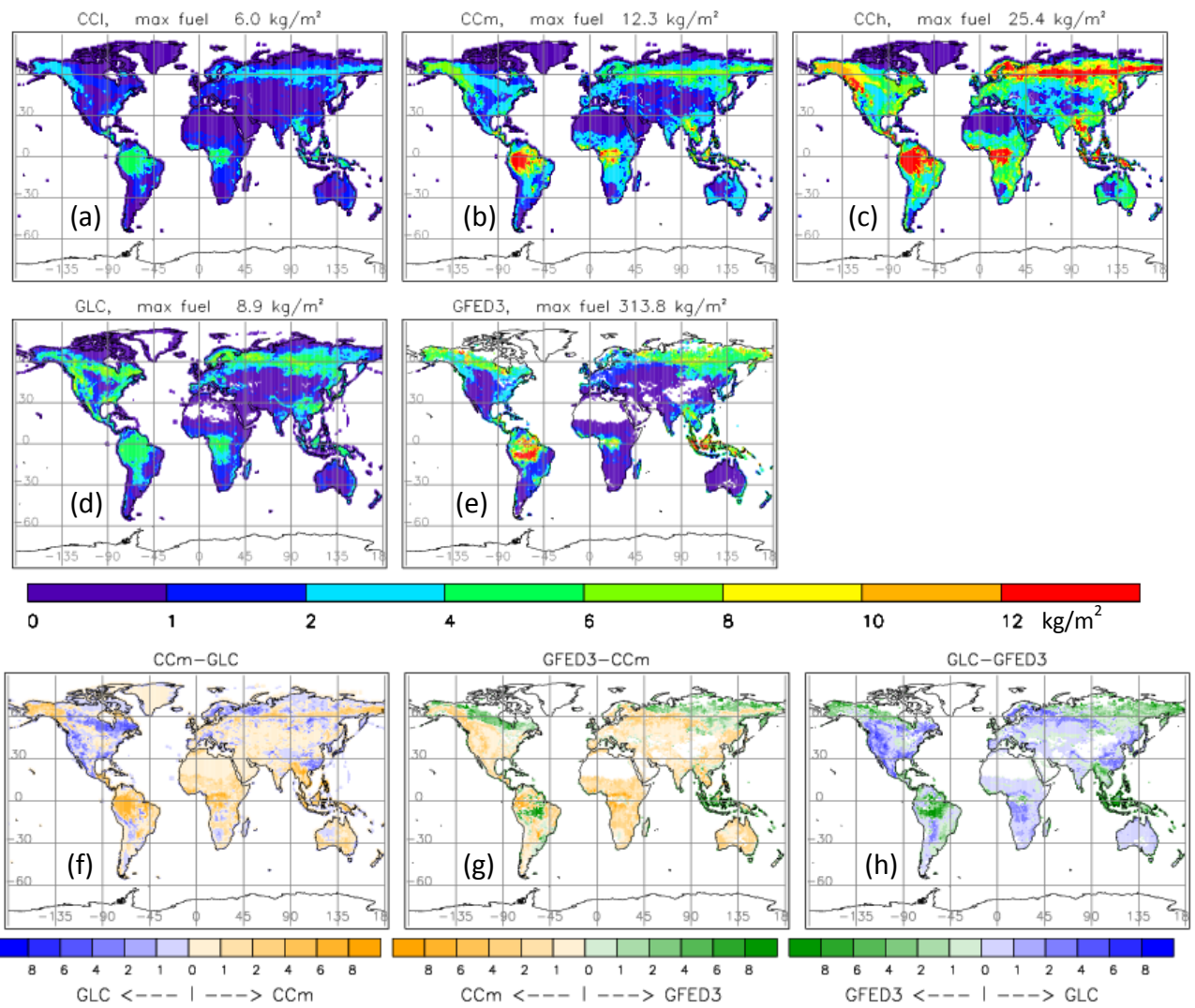


Figure 3

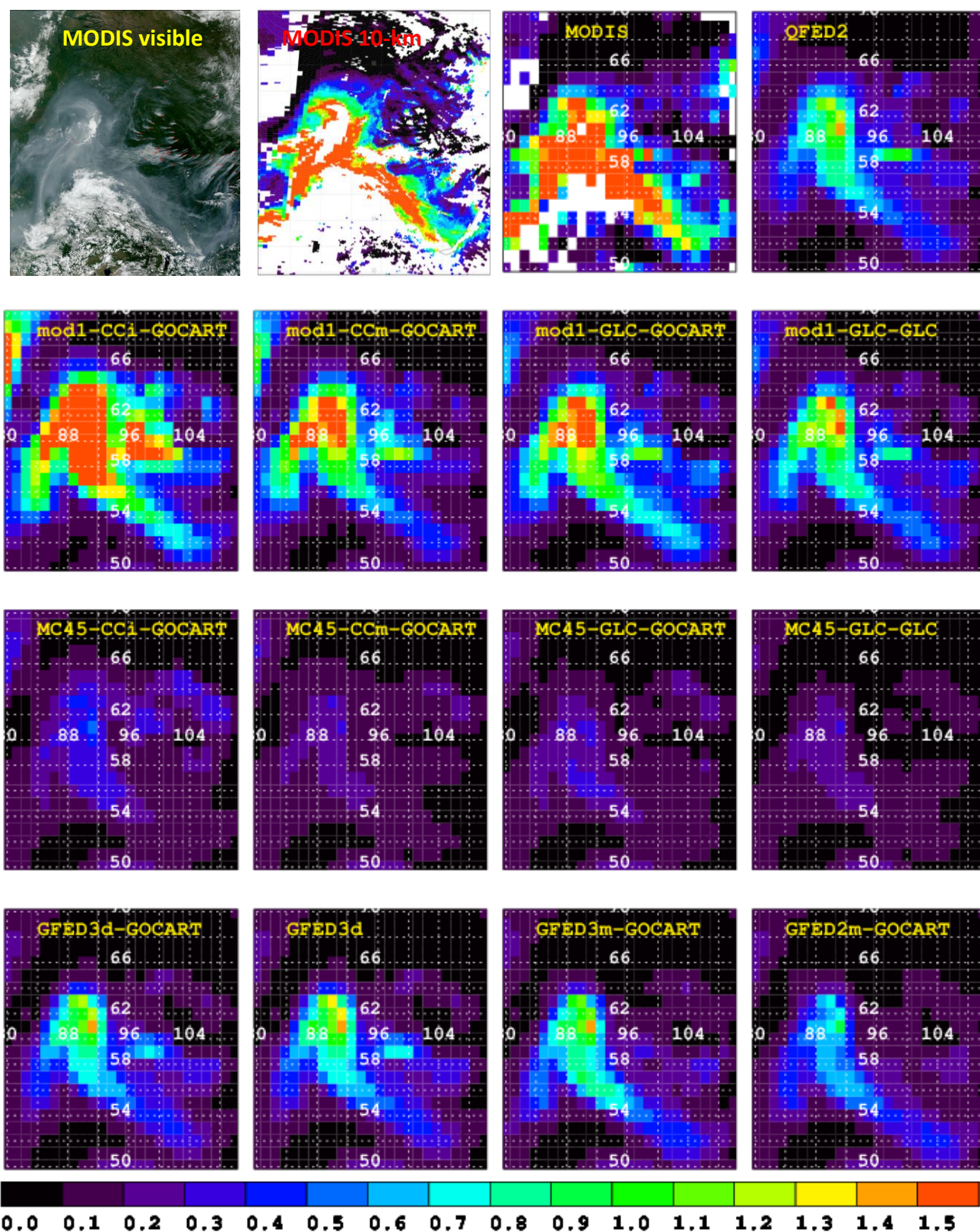


Figure 4

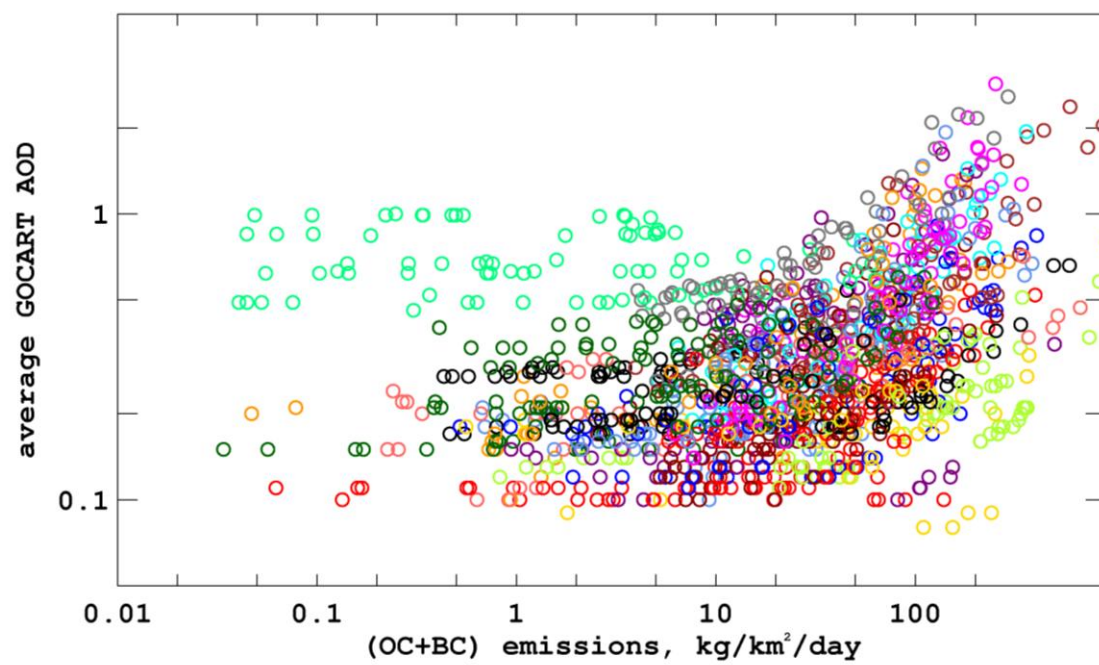


Figure 5

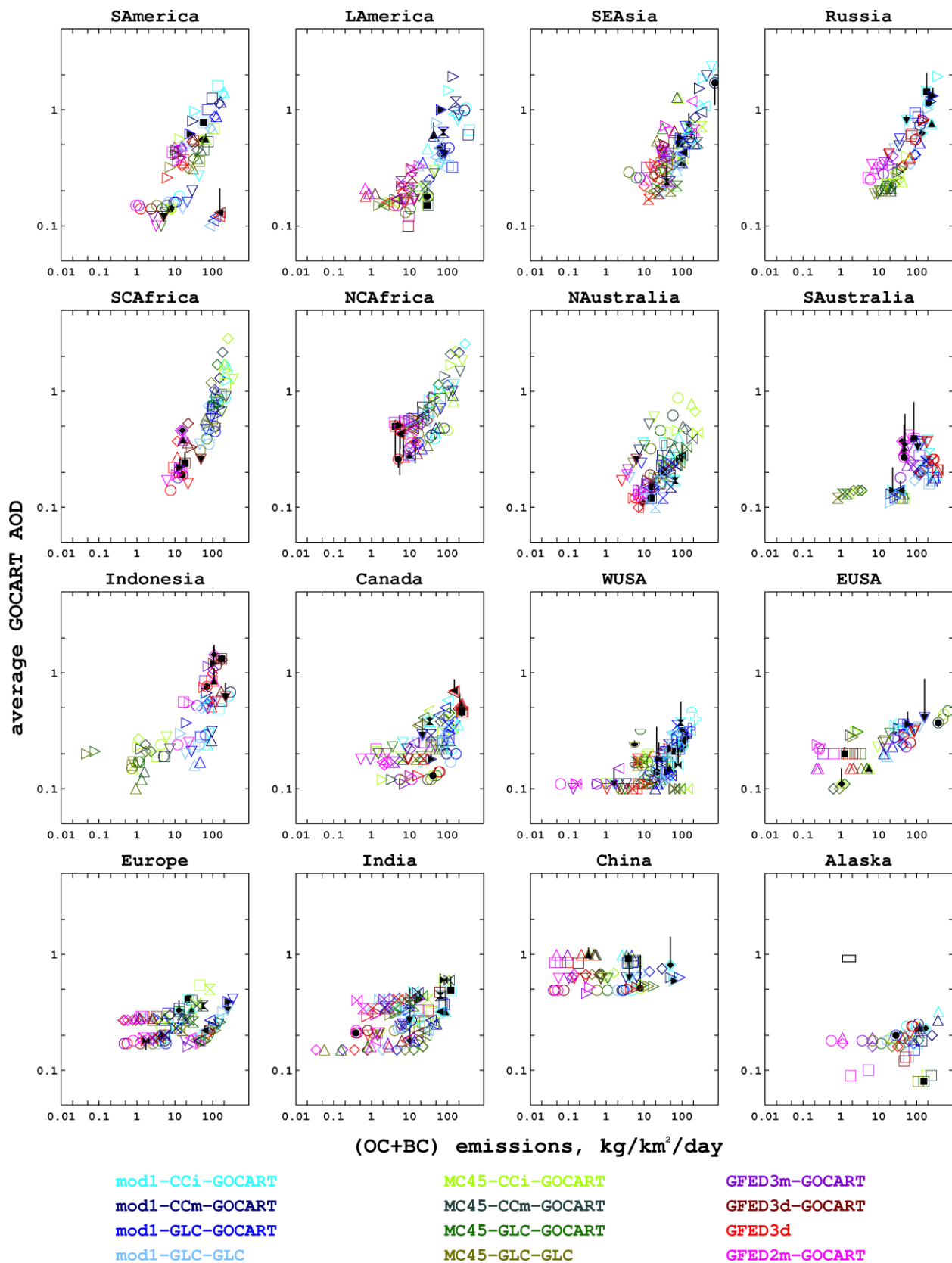


Figure 6

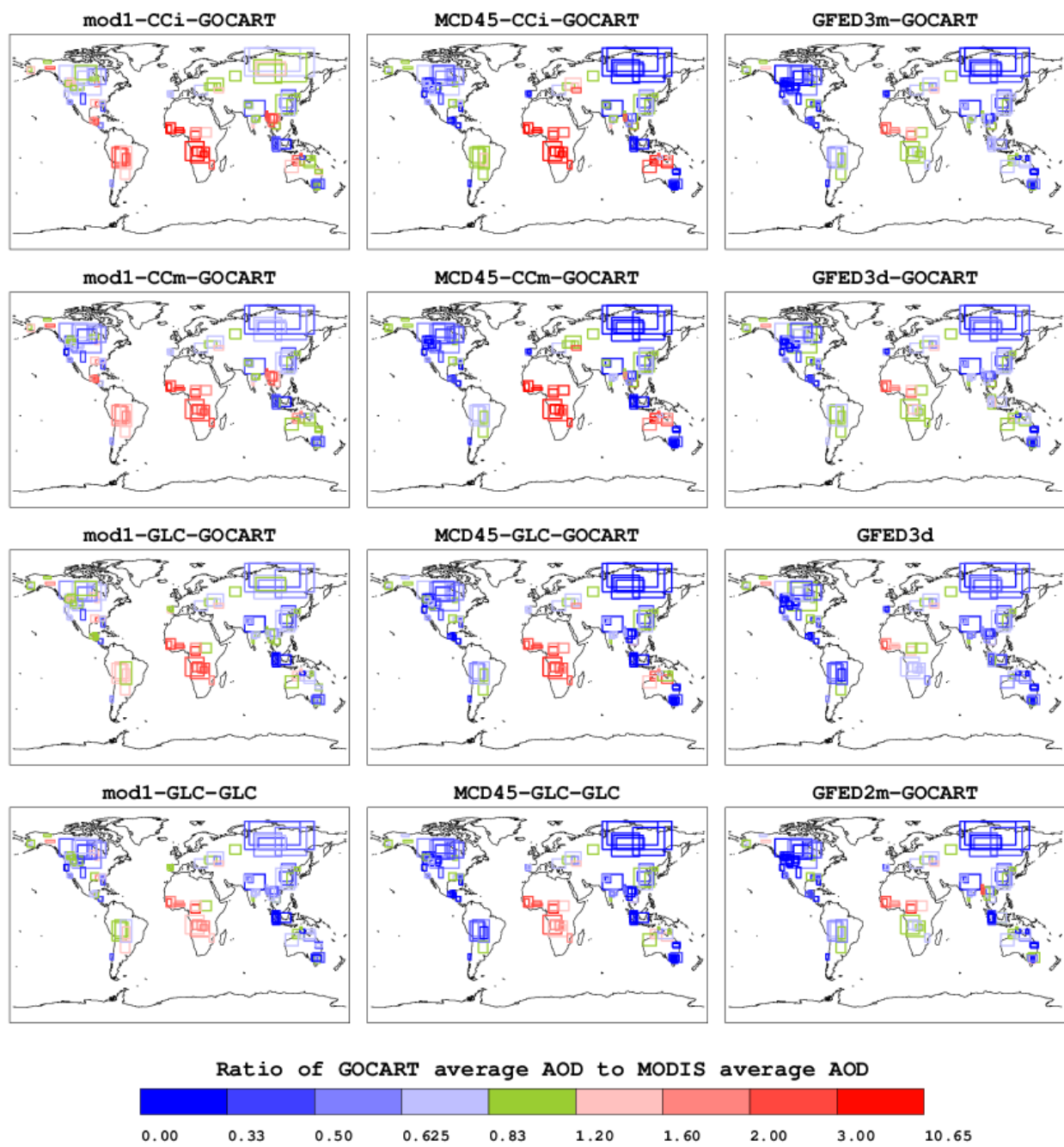


Figure 7

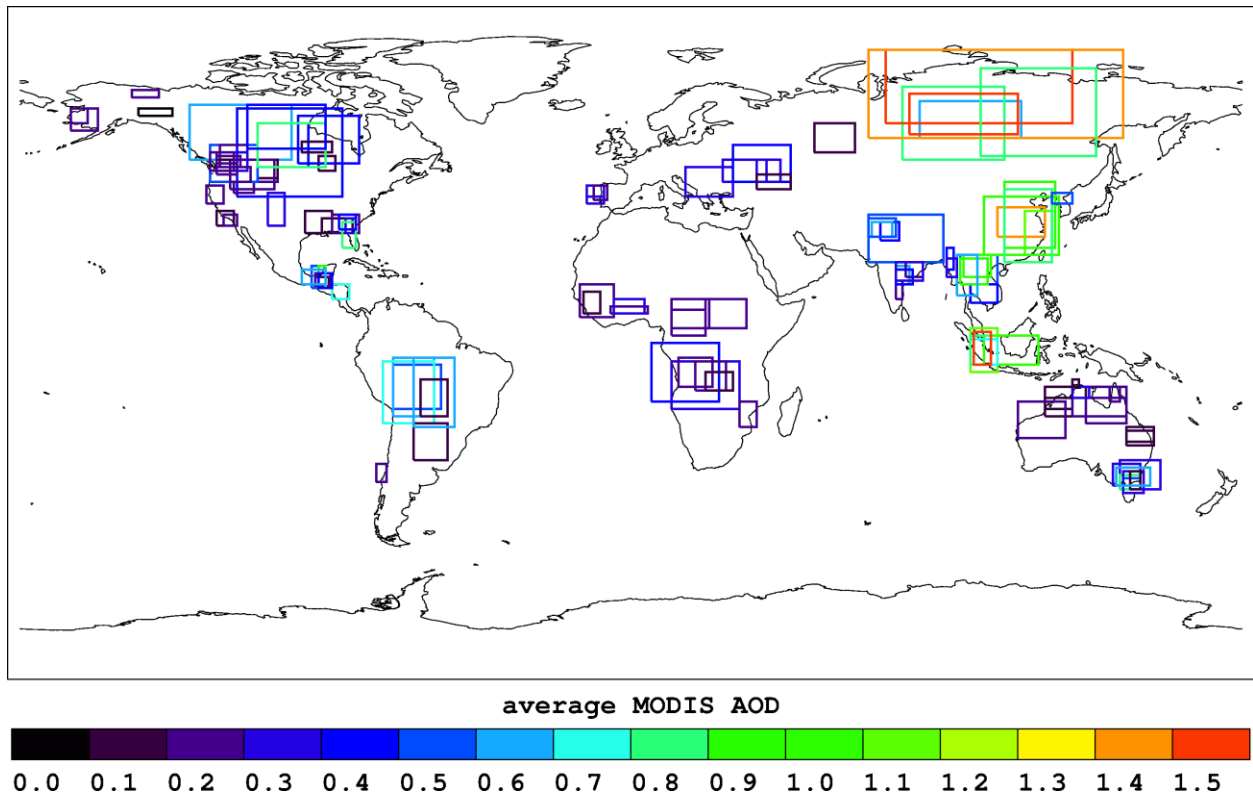


Figure 8

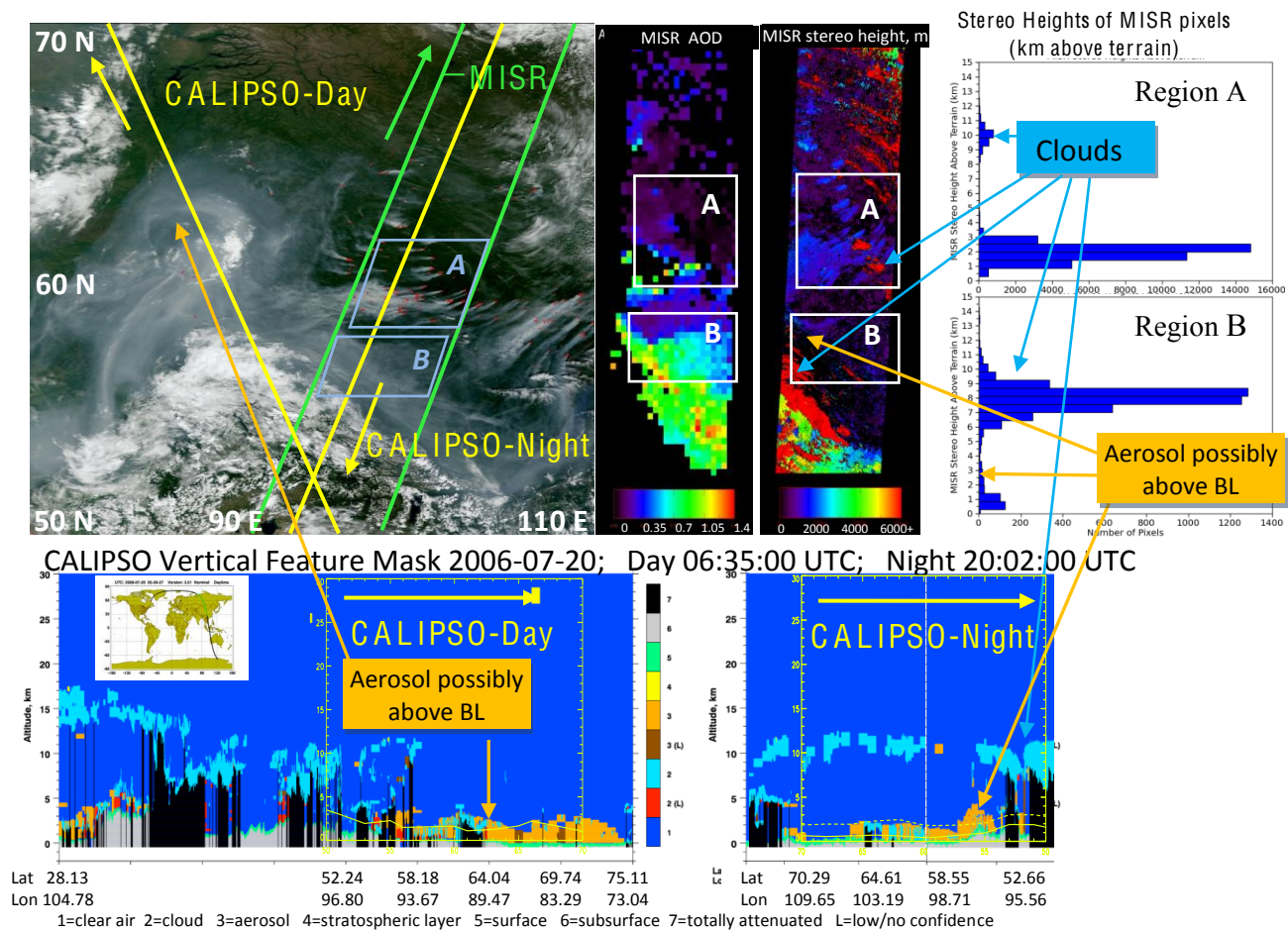


Figure 9

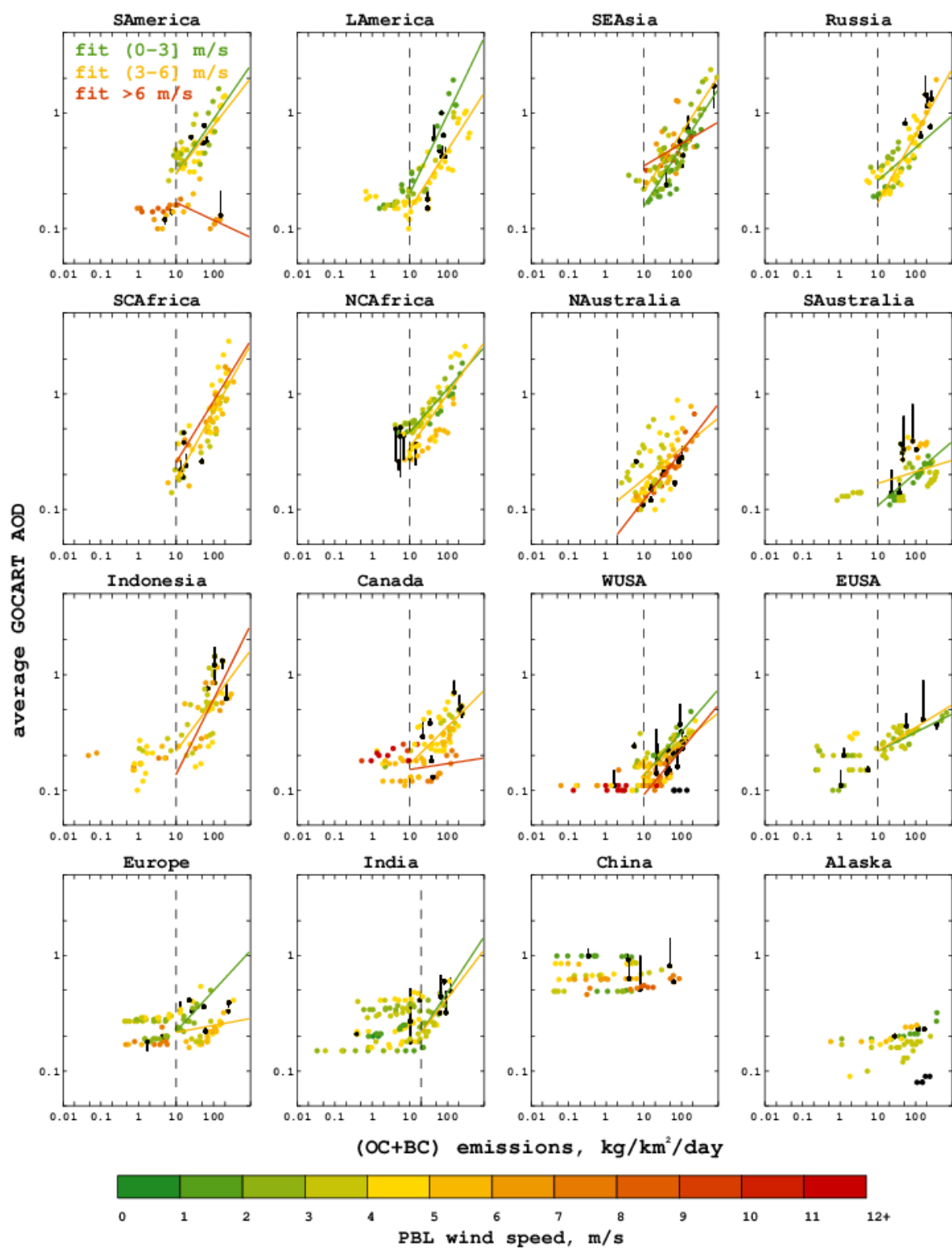


Figure 10

Table 1. GLC2000 vegetation types defined and their corresponding physical properties and emission factors [Lioussse *et al.*, 2003; Lioussse, 2010, personal communication; Michel *et al.*, 2005]

GLC code	GLC vegetation type description	Fuel density, kg/m ²	Burning efficiency	F _{BC} , g(BC)/kg(DM)	F _{OC} , g(OC)/kg(DM)	F _{SO₂} , g(SO ₂)/kg(DM)
1	Tree Cover broadleaved evergreen	23.35	0.25	0.70	6.40	0.57
2	Tree Cover broadleaved deciduous closed	20.00	0.25	0.60	6.00	1.00
3	Tree Cover broadleaved deciduous open	3.30	0.40	0.62	4.00	0.35
4	Tree Cover needle-leaved evergreen	36.70	0.25	0.60	6.00	1.00
5	Tree Cover needle-leaved deciduous	18.90	0.25	0.60	6.00	1.00
6	Tree Cover mixed leaf type	14.00	0.25	0.60	6.01	0.99
7	Tree Cover regularly flooded fresh water	27.00	0.25	0.70	6.40	0.57
8	Tree Cover regularly flooded saline water	14.00	0.60	0.65	5.15	0.46
9	Mosaic: Tree Cover / Other natural vegetation	10.00	0.35	0.61	5.00	0.68
10	Tree cover, burnt	0	0	0.00	0.00	0.00
11	Shrub Cover closed-open evergreen	1.25	0.90	0.62	4.00	0.35
12	Shrub Cover closed-open deciduous	3.30	0.40	0.62	4.00	0.35
13	Herbaceous Cover closed-open	1.43	0.90	0.62	4.00	0.35
14	Sparse herbaceous or sparse shrub cover	0.90	0.60	0.67	3.11	0.37
15	Regularly flooded shrub and/or herbaceous cover	0	0	0.00	0.00	0.00
16	Cultivated and managed areas	0.44	0.60	0.73	2.10	0.40
17	Mosaic: Cropland / Tree Cover / Other natural v.	1.10	0.80	0.64	3.64	0.36
18	Mosaic: Cropland / Shrub and/or grass cover	1.00	0.75	0.65	3.35	0.37

Table 2. GFED3 emission factors used for different fire types, in g species per kg DM [*Van der Werf et al.*, 2010]

	Deforestation	Savanna and Grassland	Woodland	Extratropical forest	Agricultural waste burning	Peat fires
OC	4.30	3.21	3.76	9.14	3.71	4.30
BC	0.57	0.46	0.52	0.56	0.48	0.57
SO ₂	0.71	0.37	0.54	1.00	0.40	0.71

Table 3. Emission estimates used as input to GOCART model

<i>Emission options (input to GOCART)</i>	mod1 -CCi -GOCART	mod1 -CCm -GOCART	mod1 -GLC -GOCART	mod1 -GLC -GLC	MCD45 -CCi -GOCART	MCD45 -CCm -GOCART	MCD45 -GLC -GOCART	MCD45 -GLC -GLC	GFED3d -GOCART	GFED3d	GFED3m -GOCART	GFED2m -GOCART	QFED
<i>Burned area products</i>													
Based on MODIS active fire counts (mod1)	X	X	X	X									
MODIS collection 5 burned area product - MCD45A1 (MCD45)					X	X	X	X					
<i>Fuel consumption, dry mass, and emission products</i>													
Carbon consumption (CC) dataset, converted to fuel consumption using Haines index (CCi)	X				X								
CC dataset, converted to fuel consumption assuming all fires of medium severity (CCm)		X				X							
GLC2000 fuel consumption (GLC)			X	X			X	X					
GFED version 3 - daily dry mass burned (GFED3d)									X	X			
GFED version 3 - monthly dry mass burned (GFED3m)											X		
GFED version 2 - monthly dry mass burned (GFED2m)												X	
QFED2 - daily BC, OC and SO ₂ emissions (QFED)													X
<i>Emission factor options</i>													
Standard GOCART F_j (GOCART)	X	X	X		X	X	X		X		X	X	
GLC2000 emission factors (GLC)				X				X					
GFED version 3 emission factors										X			

Table 4. Study cases by region with the regional specifics of biomass burning

Region Biomass burning season(s)	Case number, T/A, Date (yyyy-mm-dd) coordinates [SW corner; NE corner]	AOD threshold, symbol in Fig.5	Dominant vegetation type(s); Characteristics of burning; some notes on MODIS AOD
Alaska Jun-Aug	42 T (2006-06-04) [60N 165W; 64N 160W] 43 T (2006-06-05) [58N 165W; 64N 155W] 46 T (2006-07-23) [62N 145W; 64N 135W] 122 T (2006-06-15) [67N 147W; 69N 139W]	0.15 0.15 0.05 0.15	◇ △ □ ○ Tree cover: mosaic with other natural vegetation, evergreen; evergreen shrubs. Individual fires with associated smoke plumes. MODIS AOD is not usually retrieved in plume cores.
Canada Jun-Sep	1 T (2006-07-04) [50N 130W; 65N 100W] 2 T (2006-06-26) [48N 110W; 60N 95W] 3 T (2006-06-27) [40N 116W; 64N 85W] 31 T (2007-05-10) [47N 92W; 51N 87W] 70 A (2006-08-31) [49N 100W; 62N 80W] 74 A (2006-09-06) [52N 97W; 55N 88W] 113 T (2006-07-05) [48N 110W; 60N 90W] 114 T (2006-09-10) [53N 113W; 65N 90W]	0.15 0.15 0.15 0.1 0.15 0.1 0.15 0.15	◇ △ □ ○ ▽ ▷ ◁ ⊗ Tree cover: needleleaved, mixed leaf type, mosaic with other natural vegetation. Individual fires with associated smoke plumes combine into large-scale plumes/smoke regions. MODIS AOD is often not retrieved in plume cores.
China Jan-Apr, Aug-Oct	37 T (2007-05-29) [29N 108E; 37N 122E] 55 T (2006-08-15) [24N 116E; 36N 124E] 59 T (2006-09-22) [24N 104E; 40N 126E] 60 T (2006-10-05) [26N 110E; 44N 125E] 61 T (2006-10-30) [22N 110E; 42N 124E] 94 A (2007-04-29) [38N 124E; 41N 130E]	0.4 0.4 0.4 0.4 0.4 0.15	◇ △ □ ○ ▽ ▷ Mosaic: Cropland, tree cover, other natural vegetation; Tree cover: needleleaved, broadleaved. Many fires with no distinct smoke plumes create overall hazy/smoky area.
Europe Mar-May, Jun-Oct	51 T (2006-07-28) [40N 16E; 48N 30E] 53 T (2006-08-02) [44N 27E; 50N 40E] 54 T (2006-08-04) [44N 30E; 54N 47E] 69 T (2006-09-01) [52N 54E; 60N 66E] 85 T (2006-08-07) [38N 13W; 43N 8W] 86 T (2006-08-09) [40N 13W; 43N 8W] 87 A (2006-08-13) [39N 11W; 43N 7W] 132 A (2006-08-03) [44N 37E; 50N 44E] 133 T (2006-08-06) [42N 37E; 46N 47E]	0.2 0.2 0.2 0.15 0.15 0.15 0.15 0.15 0.1	◇ △ □ ○ ▽ ▷ ◁ ⊗ ⊗ Cultivated and managed areas; Mosaic: Cropland, tree cover, other natural vegetation. Fires with or without detectable associated smoke plumes create overall hazy/smoky area.
India Mar-May, Oct	17 T (2006-11-05) [22N 70E; 35N 92E] 41 A (2006-10-15) [28N 72E; 33N 80E] 123 A (2007-03-26) [16N 78E; 21N 82E] 124 A (2007-03-01) [12N 78E; 17N 80E] 125 A (2007-03-06) [18N 81E; 22N 86E] 126 A (2007-03-08) [16N 78E; 20N 83E] 127 A (2007-03-17) [17N 78E; 22N 86E] 128 A (2007-05-02) [29N 71E; 33N 77E] 129 A (2007-05-07) [29N 70E; 34N 78E]	0.1 0.1 0.15 0.15 0.15 0.2 0.15 0.2 0.2	◇ △ □ ○ ▽ ▷ ◁ ⊗ ⊗ Cultivated and managed areas. Fires with or without detectable associated smoke plumes create overall hazy/smoky area.
Indonesia Apr, Jul-Nov	13 T (2006-10-12) [6S 104E; 2N 120E] 14 T (2006-10-05) [6S 104E; 2N 120E] 15 T (2006-10-04) [8S 100E; 4N 108E] 16 T (2006-09-27) [6S 100E; 1N 108E] 135 A (2006-10-02) [6S 100E; 2N 106E] 136 A (2006-10-11) [6S 101E; 3N 106E]	0.2 0.1 0.15 0.15 0.15 0.15	◇ △ □ ○ ▽ Tree cover: broadleaved; cropland/shrubs and /or grass. Individual fires with associated smoke plumes combine into large-scale plumes/smoke regions. MODIS AOD is often not retrieved in

			▷	plume cores.
L America Mar-Jun	32 A (2007-05-12) [12N 88W; 16N 83W]	0.15	◇	Tree cover: broadleaved; cropland/shrubs and /or grass. Fires with or without detectable associated smoke plumes create overall hazy/smoky area.
	33 A (2007-05-13) [12N 88W; 16N 83W]	0.15	△	
	35 A (2007-04-11) [15N 93W; 18N 89W]	0.15	□	
	36 T (2007-04-11) [15N 93W; 19N 88W]	0.1	○	
	107 T (2007-05-02) [15N 94W; 21N 90W]	0.1	▽	
	108 T (2007-05-11) [15N 92W; 21N 89W]	0.15	▷	
	110 A (2007-04-18) [15N 92W; 19N 88W]	0.15	◁	
	112 A (2007-05-22) [16N 97W; 20N 90W]	0.15	⊗	
NAustralia Aug-Nov	57 T (2006-09-16) [18S 122E; 15S 130E]	0.1	◇	Shrub cover; herbaceous cover. Individual fires, some with weak associated smoke plumes. MODIS AOD is often not retrieved with intermittent clouds and bright surface.
	58 T (2006-09-18) [20S 122E; 12S 134E]	0.1	△	
	65 A (2006-11-22) [28S 146E; 23S 154E]	0.1	□	
	66 A (2006-11-22) [22S 134E; 15S 146E]	0.1	○	
	67 A (2006-11-22) [26S 114E; 16S 128E]	0.15	▽	
	68 T (2006-11-24) [20S 130E; 12S 146E]	0.1	▷	
	103 A (2007-06-10) [15S 130E; 12S 135E]	0.15	◁	
	104 A (2006-11-17) [27S 146E; 24S 154E]	0.1	⊗	
	105 A (2006-11-20) [16S 141E; 12S 144E]	0.15	⊗	
	106 A (2006-10-04) [12S 130E; 10S 132E]	0.1	⊞	
NC Africa Oct-Feb	21 A (2007-01-05) [2N 12E; 9N 22E]	0.15	◇	Tree cover: broadleaved, mixed; shrubs; cropland. Many fires with no distinct smoke plumes create overall hazy/smoky area
	62 T (2006-11-16) [4N 22E; 12N 34E]	0.15	△	
	63 T (2006-11-16) [7N 15W; 16N 5W]	0.15	□	
	64 T (2006-11-18) [4N 12E; 12N 23E]	0.1	○	
	118 A (2006-11-26) [8N 6W; 10N 5E]	0.15	▽	
	119 A (2006-11-23) [8N 5W; 12N 4E]	0.15	▷	
	120 A (2006-12-03) [8N 14W; 14N 9W]	0.1	◁	
Russia Apr-Oct	10 T (2006-07-17) [56N 85E; 66N 115E]	0.15	◇	Tree cover: needleleaved, mixed leaf type, mosaic with other natural vegetation. Individual fires with associated smoke plumes combine into large-scale plumes/smoke regions. MODIS AOD is often not retrieved in plume cores.
	11 T (2006-07-20) [50N 80E; 70N 110E]	0.15	△	
	47 T (2006-07-25) [60N 75E; 80N 130E]	0.15	□	
	48 T (2006-07-25) [56N 70E; 80N 145E]	0.15	○	
	50 T (2006-07-27) [51N 103E; 75N 137E]	0.15	▽	
	102 A (2006-07-24) [57N 82E; 68N 114E]	0.15	▷	
SAmerica Jul-Nov	38 A (2006-08-21) [18S 70W; 6S 56W]	0.15	◇	Tree cover: broadleaved evergreen, deciduous; cropland/shrubs and /or grass. Individual fires with or without associated smoke plumes, generally hazy, but some combine into larger plumes. MODIS AOD is often not retrieved in complex cloudy scenes.
	39 T (2006-08-21) [20S 70W; 4S 58W]	0.15	△	
	40 A (2006-08-24) [22S 73W; 5S 58W]	0.15	□	
	44 A (2006-07-07) [32S 64W; 22S 54W]	0.1	○	
	45 T (2006-07-12) [20S 62W; 10S 54W]	0.1	▽	
	56 T (2006-08-31) [23S 64W; 4S 52W]	0.15	▷	
	89 A (2007-01-13) [38S 75W; 33S 72W]	0.1	◁	
SAustralia Feb-May	18 T (2006-12-04) [39S 142E; 33S 150E]	0.1	◇	Tree cover: broadleaved evergreen; cropland. Individual fires with associated smoke plumes combine into large-scale plumes/smoke regions, or Fires with or without detectable associated smoke plumes create overall hazy/smoky area.
	19 T (2006-12-18) [40S 144E; 32S 156E]	0.1	△	
	20 T (2006-12-20) [40S 144E; 36S 150E]	0.1	□	
	96 T (2007-01-10) [39S 145E; 37S 150E]	0.15	○	
	97 T (2006-12-05) [41S 145E; 35S 151E]	0.15	▽	
	100 A (2006-04-13) [39S 147E; 35S 150E]	0.1	▷	
	101 A (2006-04-20) [40S 147E; 35S 150E]	0.1	◁	
	134 A (2006-12-08) [39S 143E; 34S 153E]	0.1	⊗	

SC Africa Jun-Oct	12 T (2006-06-24) [16S 6E; 0 26E]	0.15	◇	Tree cover: broadleaved. Many fires with no distinct smoke plumes create overall hazy/smoky area
	49 A (2006-07-26) [18S 12E; 5S 32E]	0.15	△	
	115 A (2007-06-24) [13S 19E; 5S 28E]	0.15	□	
	116 A (2007-06-13) [13S 22E; 8S 30E]	0.1	○	
	117 A (2006-08-04) [23S 32E; 16S 37E]	0.1	▽	
	121 A (2007-05-28) [12S 14E; 4S 24E]	0.1	▷	
SE Asia Jan-Jun , Sep-Nov	25 A (2007-03-04) [16N 97E; 24N 108E]	0.15	◇	Cropland; tree cover: needleleaved, broadleaved; shrub cover. Fires with or without detectable associated smoke plumes create overall hazy/smoky area.
	27 T (2007-01-26) [11N 100E; 16N 108E]	0.15	△	
	28 A (2007-01-28) [11N 100E; 16N 108E]	0.15	□	
	90 A (2007-04-02) [18N 98E; 24N 106E]	0.15	○	
	91 A (2007-03-13) [16N 97E; 23N 105E]	0.15	▽	
	92 A (2007-03-18) [13N 96E; 24N 102E]	0.15	▷	
	93 A (2007-03-27) [20N 93E; 26N 95E]	0.15	◁	
	95 A (2007-03-02) [18N 93E; 23N 96E]	0.15	⊗	
EUSA Feb-Jun	23 A (2007-03-07) [30N 91W; 34N 82W]	0.1	◇	Cropland; tree cover: needleleaved, broadleaved; shrub cover. Fires with or without detectable associated smoke plumes create overall hazy/smoky area.
	24 T (2007-03-07) [30N 96W; 36N 88W]	0.1	△	
	75 T (2007-03-20) [30N 88W; 35N 80W]	0.15	□	
	76 T (2007-05-20) [30N 84W; 34N 81W]	0.15	○	
	109 A (2007-05-12) [26N 85W; 33N 81W]	0.15	▽	
	111 T (2007-05-22) [1N 86W; 35N 81W]	0.15	▷	
WUSA Jun-Nov	4 T (2006-07-16) [44N 110W; 48N 104W]	0.1	◇	Three cover: needleleaved; shrub cover. Individual fires with associated smoke plumes. Heterogeneous terrain and vegetation leads to many omissions in AOD retrievals and fire detections and characterization. MODIS AOD is often not retrieved in plume cores.
	5 T (2006-07-18) [45N 110W; 50N 104W]	0.1	△	
	7 T (2006-09-12) [42N 118W; 50N 105W]	0.1	□	
	8 T (2006-06-20) [34N 107W; 41N 102W]	0.1	○	
	9 T (2006-12-03) [32N 122W; 36N 117W]	0.1	▽	
	71 A (2006-10-26) [32N 120W; 35N 116W]	0.15	▷	
	72 A (2006-08-16) [41N 117W; 44N 111W]	0.15	◁	
	73 A (2006-09-06) [44N 124W; 54N 110W]	0.15	⊗	
	77 A (2006-07-25) [46N 122W; 49N 116W]	0.1	⊗	
	78 A (2006-08-02) [48N 122W; 50N 117W]	0.15	⊗	
	79 A (2006-08-02) [38N 125W; 43N 120W]	0.15	⊗	
	80 T (2006-08-07) [48N 121W; 54N 113W]	0.15	⊗	
	81 T (2006-08-20) [47N 122W; 52N 113W]	0.15	⊗	
	82 A (2006-08-27) [47N 124W; 52N 117W]	0.15	⊗	
	83 A (2006-08-28) [48N 122W; 51N 115W]	0.15	⊗	
	84 A (2006-08-28) [44N 118W; 48N 112W]	0.15	⊗	

Table 5. Regional fit coefficients for Equation 3 by horizontal wind speed range

Region	Emission rate cutoff, kg/m ² /day	Fit coefficients (<i>a</i> ; <i>b</i>) for average wind speed ranges		
		0-3 m/s	3-6 m/s	6+ m/s
SAmerica	10	-2.29; 0.47	-2.17; 0.41	-1.43; 0.15
LAmerica	10	-3.17; 0.68	-3.08; 0.50	
SEAsia	10	-3.04; 0.51	-2.70; 0.50	-1.49; 0.19
Russia	10	-2.00; 0.28	-3.14; 0.59	
SCAfrica	10		-3.07; 0.59	
NCAfrica	10	-1.61; 0.37	-2.12; 0.46	
NAustralia	2		-2.31; 0.27	-3.08; 0.42
SAustralia	10	-2.87; 0.28	-2.02; 0.10	
Indonesia	10		-2.54; 0.44	-3.49; 0.65
Canada	10		-2.52; 0.32	-2.00; 0.05
WUSA	10	-2.80; 0.38	-2.58; 0.27	-3.29; 0.39
EUSA	10	-1.89; 0.16	-1.98; 0.20	
Europe	10	-2.32; 0.35	-1.66; 0.60	
India	20	-3.01; 0.49	-2.82; 0.42	
China				
Alaska				